A STUDY OF THE CRITICAL VISCOSITY MODEL OF FRICTION STIR WELDING IN RELATION TO TOOL FEATURES

By

Jacob Matthews

Thesis

Submitted to the Faculty of the
Graduate School of Vanderbilt University
in partial fulfillment of the requirements
for the degree of
MASTER OF SCIENCE
in
Mechanical Engineering
September 30, 2018
Nashville, Tennessee

Approved:
Alvin M. Strauss, Ph.D.
George E. Cook, Ph.D.

DEDICATION

This thesis is dedicated to my family who have supported me in everything I have done and made great personal efforts to give me opportunities they never had, to my wife for her never-ending support through all the long nights at work, and to my son William who has motivated me to work harder every day.

ACKNOWLEDGMENTS

If I was asked if I would rather be the worst player on a winning team, or the best player on a losing team, this experience has shown me the benefit of the former. To the smarter players on the team who taught me so much along the way, thank you for all your time and expertise. Gratitude is owed to Dr. Strauss and Dr. Cook for mentorship and guidance in a wider array of topics than any two people should have. Specifically, I would like to thank Todd Evans for his mentorship and overall guidance of the project, Adam Jarrell for help with instrumentation and welding support, Kelsay Neely for her unmatched knowledge of material science, and Jay Reynolds for his help with the welding program, and measuring topologies of the anvil and specimen. Finally, the project would not have been possible without the financial support of Vanderbilt University and the NASA Space Grant.

TABLE OF CONTENTS

Page

Chapter

LIST OF TABLES

Table Page

LIST OF FIGURES

1. Introduction

Friction Stir Welding (FSW) was patented in 1998 by The Welding Institute in Cambridge, England. [1] Friction Stir Welding is a steady-state process utilizing a rotating, axially-loaded tool to create friction to form a solid-state bond. The non-consumable tool commonly has a shoulder and pin. The shoulder is the surface that distributes much of the axial force to the material, and the pin is a raised cylinder in the center of the shoulder that is used to plastically deform the materials being welded. Common control parameters of friction stir welding are tool rotation rate, the plunge depth of the tool, and the traverse rate of the tool in relation to the material. Other process parameters include heat flux, torque, axial force, transverse force, and strain rate. Figure 1 shows the components and process of FSW. [2]

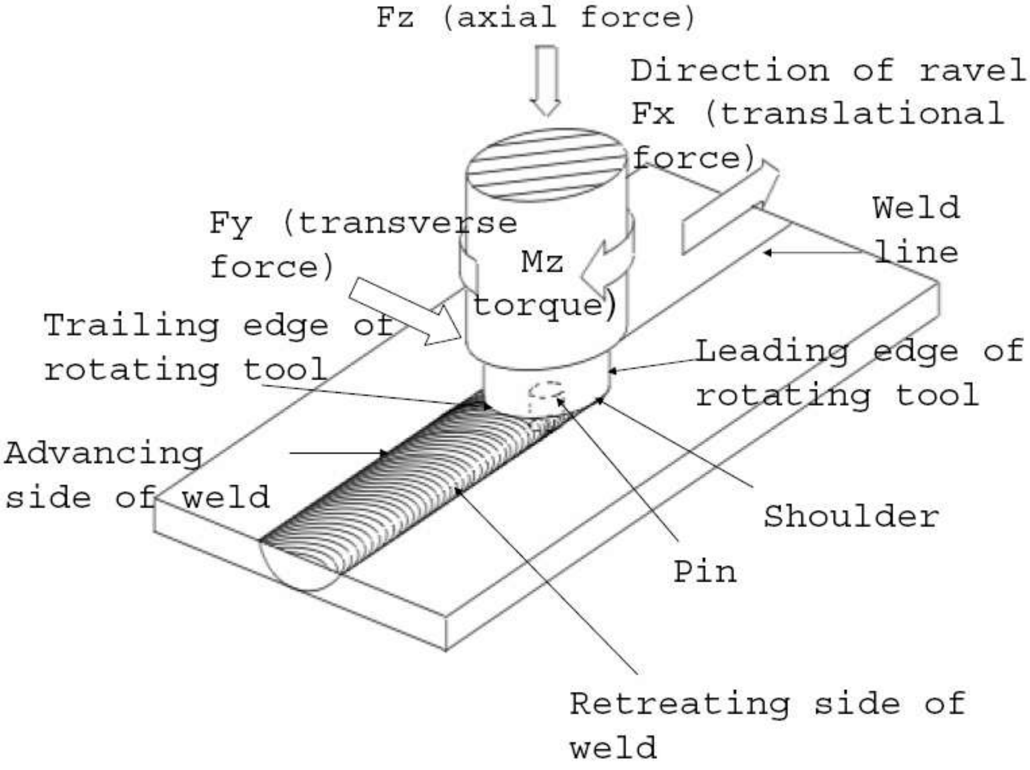

Figure 1 - FSW Components

FSW has demonstrated the ability to join materials with less weight, less energy, fewer restrictions, and at higher strengths. FSW does not require filler materials, resulting in welds that weigh less than traditional methods. This weight reduction and the ability to join higher strength alloys like the 2000 and 7000 series of aluminum alloys makes FSW popular in the aerospace industry. FSW requires less energy and is cheaper to operate than traditional methods requiring large power supplies and filler materials. FSW is not restricted by materials, as it easily welds materials difficult or impossible to weld using traditional methods like certain aluminums or dissimilar metals. This makes welding of aluminum components to steel frames economical in the automotive industry. The possibility of welding under water has been demonstrated and theoretically possible in space, making it popular in the marine and space industries.

This thesis will discuss the basics of FSW modeling and layout the progress of FSW models over time. This will include the progress of heat generation, material flow, the eventual addition of localized material flow bands, and how weld seam input energy affects the thermomechanical conditions of the weld. Welding parameter maps will be introduced that help estimate correct welding parameters and how weld strengths are affected. The thesis will then discuss tool features and how they may affect the thermomechanical conditions of the weld in the context of the models and weld parameter maps discussed. To do this, it will explore a simplified pseudo-model based on the idea that there is a critical viscosity that determines if the material will flow and conduct several welds to verify that this model can predict the width of material flowing around the pin. It will then outline the experiments conducted with four different tool designs, discuss the results of these welds, and draw conclusions on how tool features affect the thermomechanical conditions and strengths.

2. Heat Generation and Flow Modeling

2.1 Rosenthal Solutions

Rosenthal developed a thermal model for traditional arc welding. His model described quasi-steady state temperature fields in a semi-infinite plate from a moving, line heat source. [3] The Rosenthal equation is described in Equation 1. [3]

$$T = T_\infty + \frac{Q * \exp(\frac{-v * \left(w_{fb} + r\right)}{2\alpha})}{2\pi k r}$$

Equation 1 - Rosenthal Equation

$Q \equiv heat\ generation$
$v \equiv transverse\ velocity$
$r \equiv distance\ from\ heat\ generation\ source\ (pin\ axis)$
$\alpha \equiv thermal\ diffusivity$
$k \equiv thermal\ conductivity$
$w_{fb} \equiv flow\ band\ width$

Equation 2 describes the Peclet number. It describes the relative rates of heat transfer by convection and conduction to determine if heat transfer is dominated by convection or conduction. If this value is much less than one, it means that isotherms around the pin become near circular and Rosenthal's solutions are valid. Values greater than one indicate that forced convection occurs at a significant magnitude. [4] [5]

$$Pe = \frac{\rho v_t C_p L_R}{k} = \frac{v_t p_r}{2\alpha_0}$$

Equation 2 - Peclet Number

$\rho \equiv material\ density$
$v_t \equiv transverse\ velocity$
$C_p \equiv specific\ heat$
$L_R \equiv characteristic\ length\ of\ boundary\ layer\ thickness$
$k \equiv thermal\ conductivity$
$p_r \equiv pin\ radius$
$\alpha_0 \equiv thermal\ diffusivity\ at\ base\ plate\ at\ critical\ temperature$

When FSW is referred to as a solid-state welding process, it distinguishes it from traditional arc welding. In traditional arc welding, extreme heat creates a liquid form of the materials to be joined. Several unwanted effects may result. Liquifying the materials significantly changes the microstructure and lowers the weld strength. The extreme heat also creates high residual stresses in the materials. This process does not work for some metals and does not work for many dissimilar metals and plastics. Solid-state welding joins materials that maintain their form as a solid. FSW does this by maintaining temperatures under the material’s solidus temperature and applying pressure and high strain rates.

Modeling the process of FSW has proven elusive over its almost three-decade history, despite the dramatic increase in computing power over the same time. It is understood that the material state is in a plastic region somewhere between solid and liquid. Some techniques have tried to adapt solid mechanics techniques to describe the process, and some have tried adapted fluid mechanics approaches. Two main questions dominate the modeling efforts today: Is the peak temperature dominated by heat generation from friction or plastic dissipation and is material plasticized by the formation of adiabatic shear bands or a decrease of viscosity below a critical value?

The dominant question in thermal models is whether the peak temperature is dominated by heat generated from friction or plastic dissipation. Another way to characterize this question is by determining the velocity of material at the tool interface. Three described possibilities are: sticking, slipping, or partial sliding and sticking.

2.2 Schmidt and Hattel Heat Generation Model

In a slipping condition, the material velocity near the tool is zero, meaning the tool rotation does not cause any deformation and only creates frictional heat caused by the contact of two metals sliding past each other. This condition will occur if the contact shear stress is less than the material yield shear stress. The material will deform slightly but will remain elastic. [6]

In a sticking condition, a boundary layer of material is formed around the pin. The material nearest the tool travels the same speed as the tool, creating a boundary layer of intermediate velocities within a band until the material velocity is zero again. This condition is valid where the frictional shear stress is greater than the yield shear stress of the material. [6]

In the remaining possible condition, a combination of both are present. Like in the sticking condition, a boundary layer is created in the material. Unlike the sticking condition, the velocity of material nearest the pin will be traveling at a velocity below the tool velocity. In this case, a dynamic contact shear stress equals the material shear yield stress and comes to an equilibrium dependent on the plastic deformation rate. [6]

The contact state variable, δ, describes whether the tool is sticking, slipping, or the amount of partial sticking. It is defined as the material velocity nearest the pin divided by the tool velocity, Equation 3. [6]

$$\delta = \frac{v_{material}}{v_{tool}}$$

Equation 3 - Contact State Variable

A value of one would describe sticking, while a value of zero would describe slipping. Schmidt et al concluded that the contact state variable was one or very near one, indicating that a sticking condition is most likely [6].

Schmidt and Hattel are often cited for developing the generally adopted equation for total heat generation, Equation 4. [6]

$$Q_{total} = \delta Q_{sticking} + (1-\delta)Q_{sliding}$$
$$= \frac{2}{3}\pi\omega\left[\delta\tau_{yield} + (1-\delta)\mu p\right]\left[\left(R_{shoulder}^3 - R_{probe}^3\right)(1-\tan\alpha) + R_{probe}^3 + 3R_{probe}^2 H\right]$$

Equation 4 - Heat Generation Equation

$\delta \equiv Contact\ State\ Variable\ (dimensionless\ slip\ rate)$
$\tau_{yield} \equiv Material\ Yield\ Stress\ at\ welding\ temperature$
$\mu \equiv$ Friction Coefficient
$p \equiv$ Uniform Pressure at contact interface
$\omega \equiv Angular\ Rotation\ Speed$
$\alpha \equiv Cone\ Angle$
$R_{shoulder} \equiv Shoulder\ Radius$
$R_{probe} \equiv Probe\ or\ Pin\ Radius$
$H \equiv Probe\ or\ Pin\ Height$

This early research recognized that as the temperature approaches the solidus temperature and acts more like a liquid, the yield stress decreases and consequently generates less heat. While Schmidt and Hattel's model neglects strain-rate dependence in the material flow model, they identified that the process is self-regulating to a degree. Heat from plastic dissipation depends on the material's flow stress at the current temperature, the strain, and the strain rate. The contact stress will be equal to the material yield shear stress during steady-state conditions. [7]

Assuming a sticking condition, the contact state variable equals one and the contact shear stress is estimated to be the material yield stress divided by the square root of three. Equation 5 represents the resulting equation for heat generation assuming a sticking condition for a flat shouldered, threadless pin tool. [6]

$$Q_{total} = \frac{2}{3}\pi\omega\frac{\sigma_{yield}}{\sqrt{3}}\left[\left(R_{shoulder}^3 - R_{probe}^3\right)(1-\tan\alpha) + R_{probe}^3 + 3R_{probe}^2 H\right]$$

Equation 5 - Heat Generation from Sticking Condition

Separating Equation 5 into heat generation from shoulder, probe shoulders, and probe bottom allows contributions from each to be quantified. Schmidt and Hattel determined heat generation to be 83% from the shoulder, 16% from the probe sides, and 1% from the probe tip for AL 7075 and 86% from the shoulder, 11% from the probe sides, and 3% from the probe tip for AL 2024 [7]. Analytical estimates for tools with threaded probes by Colegrove estimate heat generation from the probe as high as 20%. [8]

2.3 Mendez Heat Generation Model

Mendez et al. noted that the heat generation from the shoulder does not significantly affect the peak temperature near the pin. The shoulder acts as a distributed, pre-heating mechanism that initially softens material, but does not significantly affect the plasticization of the metal. The peak temperature is dominated by plastic dissipation by the pin. This insight allowed modeling to uncouple shoulder heat generation from pin plastic dissipation heat generation. [5]

3. Material Flow Modeling

3.1 Colligan Material Flow Experiments

Colligan first attempted to measure material flow by imbedding steel balls into a butt weld of AL 6061 and AL 7075 to act as tracers. Steel balls that struck the pin on the advancing side of the weld were deposited on the retreating side behind the pin. Steel balls that struck the pin on the retreating side of the weld were also deposited on the retreating side behind the weld. Small vertical displacements towards the shoulder were observed. He concluded that material flow behind the pin was characterized by both "stirring" and extrusion. The material on the advancing side was stirred into the void by the pin, and the material on the retreating side was extruded between the pin and the parent material. [9]

3.2 Reynolds Material Flow Experiments

Reynolds used a similar tracer technique but used thin sheets of AL 5054 during a butt weld of AL 2195. He used the data to create 3D maps of the flow to improve visualization of the material flow. He concluded that the material was extruded on both sides of the pin and that the role of the pin was to provide frictional heating to create the conditions for successful extrusion. [10]

3.3 Arbegast Extrusion Model

Arbegast suggested an extrusion model that divided the material up into four zones. Zone I was material on the advancing side near the pin, Zone II was material on the retreating side near the pin, Zone III is material dominantly influenced by the shoulder, and Zone IV was the material underneath the pin he called the "Vortex Swirl Zone". The zones were coupled into a system where motion of material from one zone affected motion of material in an adjacent zone. [11]

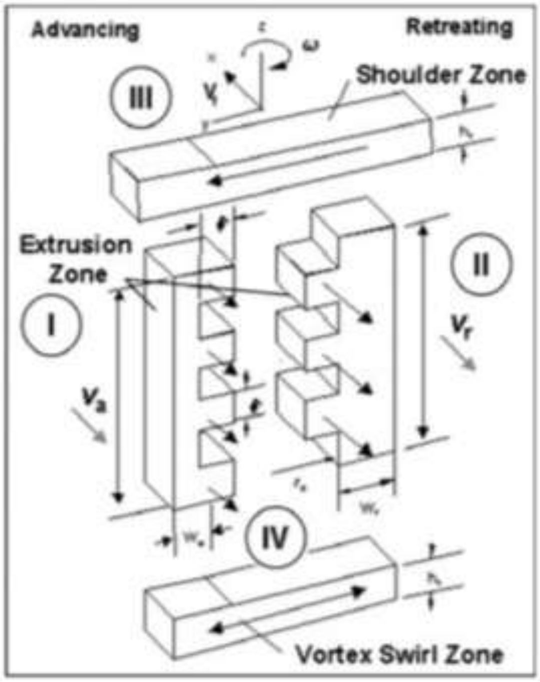

Figure 2 - Arbegast Flow-Partitioned Zones

3.4 Ulysse Material Flow Model

Ulysse introduced a model that related the deviatoric stress tensor to the strain-rate tensor. This assumes that the material is a rigid-visco-plastic material highly dependent on temperature and strain rates. This led to the conclusion that flow stress is the requirement driving material flow, and that it can be solved for using an inverse hyperbolic-sine relationship and the Zener-Hollomon parameter [12]. The Zener-Hollomon parameter represents temperature-compensated strain rate [4]. This method was used by Sellars and Tegart [13] and was modified by Sheppard and Wright [14]. It treats the material like a viscous non-Newtonian fluid with negligible strain hardening effects. [15]

3.5 Nunes Rotating Plug Model

Nunes et al. suggest that a “plug” of material rotates at the same velocity as the pin and travels with the tool. The width of this plug of material is at a maximum at the retreating edge and can be approximated by Equation 6.

$$w_{sb} = \frac{2v_t}{\omega}$$

Equation 6 - Nunes Shear Band Width [16]

The idea that material is rotating with the pin has been widely accepted, though the cause has not been agreed upon. The different models can be categorized as adiabatic shear bands, Couette flow, and viscosity. These models are summarized in the following sections.

3.6 Pei and Dong Adiabatic Shear Band Model

Adiabatic shear bands are possible in materials with microstructural inhomogeneities or defects. [17] For example, pure aluminum does not have microstructural inhomogeneity, and has not been reported to experience shear bands. Aluminum alloys create microstructural inhomogeneities and allow shear bands to form. High strain gradients are a principal cause for shear band formation. Observations suggest that high strain rates cause massive elongation of grains along the shear band propagation path, orientation of the elongated grains along shear flow direction, and eventual fragmentation of the grains into smaller grains. [17]

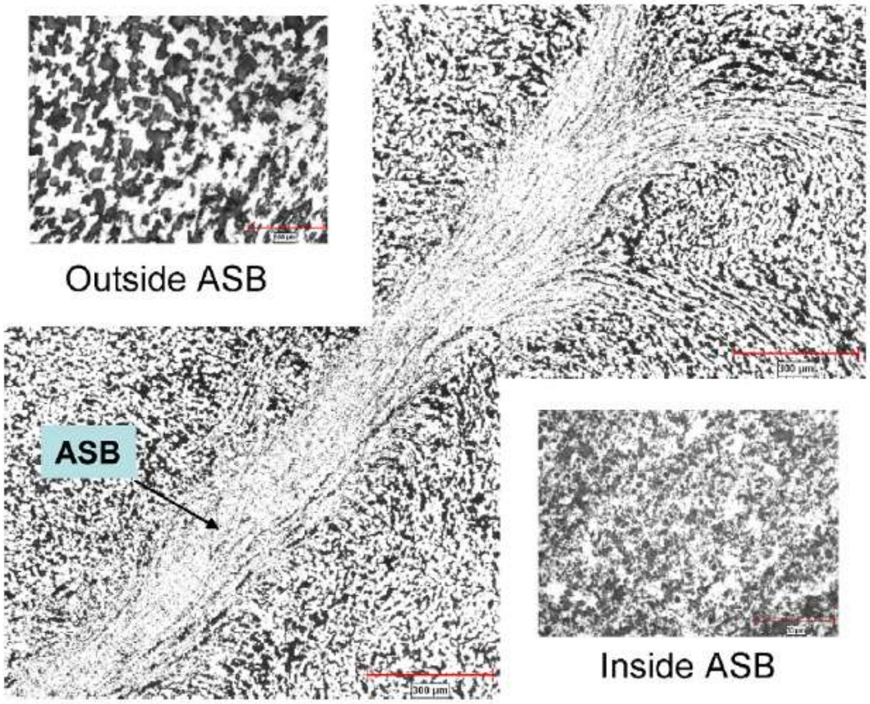

Figure 3 - Adiabatic Shear Banding Grain Structure

A significant increase in the material strength over strain rates of about 10,000 s^{-1} occurs and is caused by a change in dislocation motion mechanism. At low strain rates, the deformation rate is thermally activated. At these low strain rates, influence of the temperature of the material on flow stress can be neglected. At high strain rates, the glide kinetics are controlled by viscous phonon and electron drag. [18] This means at high strain rates, heat generation due to plastic dissipation occurs and thermally softens the local material. Since flow stress is dependent on temperature and strain rate, multiple phenomena are present.

The flow strength increases due to higher strain rates but decreases due to temperature. Overall, the local rise in temperature due to plasticization dominates and greatly reduces the flow stress where strain rates are high. This means that shear bands require strain rates of greater than 10,000 s^{-1} to form. [18] Shear bands are highly influenced by the strain hardening ability of the material. A material with a higher strain hardening ability requires a higher temperature for thermal effects to start dominating strain rate effects and vice versa. [19] Adiabatic shear bands are harder than the associated bulk material but are also more prone to cracking. They can be eliminated from a material's microstructure through heat treatment. [17]

Pei and Dong initially assumed that the material behavior can be modeled by the Johnson-Cook law because of its dependency on temperature, strain, and strain rate. This model predicted temperatures above the melting point of the material which experimental results show to be unlikely. They suggest that this temperature increase is from the strain-hardening term, which hot forming research has found to be minimal at temperatures present in FSW. [19]

Pei and Dong proposed an interesting model of shear localization in relation to FSW parameters. They only considered the process during one revolution of the tool at steady state. As the tool begins its rotation, the slipping condition is assumed. Frictional heat generation causes thermal softening according to the Zener-Hollman model and the material near the pin begins to change to a sticking condition. The velocity of the material near the pin quickly approaches the velocity of the tool causing high strain and strain rates. The heat generation due to Coulomb friction disappears and localized heat generation due to plastic dissipation dominates.

The localized plastic heat generation continues to plasticize material and the width of the shear band of material traveling at the velocity of the pin increases. To satisfy mass balance and continuity conditions, the width of the shear band must be greater than or equal to the width of the void created by the pin. If the shear band width is less than the max material flow, void defects are predicted. [20]

3.7 Crawford Couette Flow Model

Crawford compared a traditional thermo-viscoplastic model to a Couette Flow model originally developed by North et al. The Couette Flow Model is a fluid mechanics approach that describes the flow of a viscous fluid between two plates. In the case of friction stir welding, the plates are concentric cylinders. The inner cylinder is the tool, and the outer cylinder is the parent material. The distance between the two plates is the width of the "third body region", what is referred to in this thesis as the shear band thickness. This distance is described by Equation 7. [2]

$$W_r = \frac{\alpha}{\beta\varphi^2 + r_p\varphi + 1}$$

Equation 7 - Crawford Third Body Region Width

$$\alpha = \frac{1}{2(r_p - \lambda\delta^2)}$$

$$\beta = \frac{r_s^2 - r_p^2}{h_p\lambda}$$

$$\varphi = \frac{\omega}{v_f}$$

$$\delta^2 \equiv projected\ thread\ area$$

$$\lambda \equiv number\ of\ threads\ per\ inch$$

Crawford also modeled the torque in FSW. The welding power is equal to the torque multiplied by the rotation rate. The welding torque can be broken down to represent torque from the pin and torque from the shoulder. The first term of Equation 8 represents torque from the shoulder, and the last two terms represent the torque contribution of the pin. [2]

$$M = \int_{r_p}^{r_s} 2\pi r\sigma\, dr + 2r_p^2 h_p\sigma + \int_0^{r_p} 2\pi r^2\sigma\, dr$$

Equation 8 - Welding Torque

$$\mathrm{r} \equiv \mathrm{radius}$$

$$\sigma \equiv axial\ stress$$

$$r_p \equiv pin\ radius$$

$$h_p \equiv pin\ height$$

$$r_s \equiv shoulder\ radius$$

If we neglect the torque from the pin's bottom as negligible, then the torque from the pin is represented by Equation 9. [2] Crawford concluded that the pin's contribution to torque represented roughly a fourth of the total torque required by the machine.

$$M_p = 2r_p^2 h_p \sigma$$

Equation 9 - Torque Contribution of Tool Pin

Crawford ultimately concluded that the Couette Flow Model works best for high weld pitch welds, defined as the rotation rate divided by the translational rate. Overall, the visco-plastic model was more accurate over a broad range of weld pitches. At higher weld pitches, the Couette flow becomes more predictive than the visco-plastic model high temperatures increase the material's ability to flow. Couette flow likely works best as material acts more like liquid, but less at lower temperatures.

3.8 Nandan Critical Viscosity Model

Nandan proposed a model for material flow that is dependent on the viscosity of the material. The temperature and strain rate of the material lower the viscosity of the metal until a critical viscosity is reached allowing material to flow. Once the material flows, forces on the material are released, temporarily lowering both temperature and strain rates until the viscosity rises above the critical viscosity and the process restarts. The iterative process results in the banded structure known as onion rings behind the weld zone. [4]

Viscosity can be found with just knowledge of the flow stress and strain rate in Equation 13 and Equation 16. The viscosity was found to be dependent on both strain rate and temperature, but strain rate was a more dominant factor for FSW thermo-mechanical conditions. Nandan et al. determined the critical viscosity for AL6061-T6 to be 5x10^6 Pa-s. This value was confirmed by Franke et al. [21]

$$\mu = \frac{\sigma_f}{3\dot{\varepsilon}}$$

Equation 10 – Viscosity

$\dot{\varepsilon} \equiv$ strain rate
$\sigma_f \equiv$ flow stress

The critical viscosity model is differentiated from the adiabatic shear band model by the method of material transport. While strain rate contributes to material flow for both models, adiabatic shear bands suggest strain rate dominates the material flow process and causes a change in dislocation mechanism and is influenced by strain hardening. FSW likely involves a range of microphysical processes involved in both elastic and anelastic deformation. [22] The critical viscosity model suggests more of a balance between strain rate and temperature that is thermally activated by the heat generated by plastic dissipation and is not affected by strain hardening. Small shear bands may be forming, but they are on a small scale and do not dominate material flow.

3.9 Johnson-Cook Model

There are many models of material strength at high pressures and strain rates. Johnson-Cook, Zerilli-Armstrong, mechanical threshold stress, thermal activation phonon drag, Steinberg-Lund, Steinberg-Guinan, and Preston-Tonks-Wallace to name a few. [23] Most research in relation to FSW has focused on the Johnson-Cook model because of its applicability to high strain rate loading and its ease of use. The Johnson-Cook model determined material parameters over a relatively low range of strain, strain rate, and temperature data. This leads to yield stresses much larger than experimental data at plastic strain values of 100-200 at room temperature. This suggests that the Johnson-Cook is a strain hardening dominated material model, but hot forming research suggests that material at temperatures approximate to FSW show little evidence of strain hardening ability. [19] Assuming that plasticization is occurring, then Equation 11 represents the flow stress according to the Johnson-Cook model. [18]

$$\sigma_f = (A + B\varepsilon_{pl}^n)(1 + C\ln\frac{\dot{\varepsilon}_{pl}}{\dot{\varepsilon}_0})(1 - T^{*m})$$

Equation 11 - Flow Stress

$A \equiv$ elastic limit strength
$B, C, n, m \equiv$ empirical fit constants
$T^* \equiv$ homologous temperature (ratio of temperature to melting temperature)
$\varepsilon \equiv$ effective plastic strain
$\dot{\varepsilon} \equiv$ effective plastic strain rate

3.10 Zener-Hollomon Parameter and Hyperbolic-Sine Model

Ulysse introduced a model that related the deviatoric stress tensor to the strain-rate tensor. This assumes that the material is a rigid-visco-plastic material highly dependent on temperature and strain rates. This lead to the conclusion that flow stress is the requirement driving material flow, and that it can be solved for using an inverse hyperbolic-sine relationship and the Zener-Hollomon parameter. [12] The Zener-Hollomon parameter represents temperature-compensated strain rate. [4] This method was used by Sellars and Tegart [13] and was modified by Sheppard and Wright [14]. It treats the material like a viscous non-Newtonian fluid with negligible strain hardening effects. The temperature is calculated using Equation 1.

$$Z = \dot{\varepsilon}e^{\frac{Q}{RT}}$$

Equation 12 - Zener-Hollomon Parameter

$\dot{\varepsilon} \equiv$ strain rate
$\mathrm{Q} \equiv$ temperature − independent activation energy
$R \equiv$ gas constant
$T \equiv$ temperature

$$\sigma_f = \frac{1}{\alpha}\sinh^{-1}(\frac{Z}{A})^{\frac{1}{n}}$$

Equation 13 - Hyperbolic Sine Relationship for Flow Stress

$\alpha \equiv thermal\ diffusivity$
$n, A \equiv empirical\ fit\ constants$

3.11 Onion Rings

The banded structure left behind welds is often referred to as “onion rings”. The banded structure is formed by alternating layers of high strain rate bands and average strain rate bands deposited into the void behind the pin. [24] These different bands have also been explained by high strain rate bands on the advancing side of the weld and extruded material on the retreating side of the weld. [25]

At high rotational rates and low transverse rates, onion ring structures cover a small width of the weld and have irregular material flow including chunks of sheared parent material. As translational rate increases, material flow becomes more regular and onion ring structures extend further across the weld until an optimal translation rate is reached and then begin to recede. [26]

Onion ring bands have thickness approximately equal to tool's transverse advance per revolution for cylindrical tools. This thickness is divided by the number of faces of the pin for non-cylindrical tools (three for triangular tools for example). [24] When this value is small, the distance between onion ring bands is small and it is difficult for the plasticized material to be deposited because the area between the tool and the previous band is too small. As this value increases, more plasticized material can be deposited across the width of the weld. This phenomenon depends mainly on the shape of the tool's pin and not on whether a sticking or slipping condition is present. [26]

Onion ring structures start on the retreating side and compete with tunnel defects originating on the advancing side of the weld. More pronounced onion ring structures mean fewer tunnel defects in the weld. After material passes by the pin, the void behind the pin creates a "low pressure zone" that exerts a force on the material towards it. If the material is not fluid enough to flow into the void, void defects are formed. More pronounced onion rings may signal that enough plasticized material is being produced to fill the void behind the pin and avoid tunnel defects. [24]

An oscillation in the axial force applied to the material occurs during welding. The frequency has been found to be equal to the rotation rate per second times the number of faces of the tool (i.e. 1 for a circle, three for a triangle). This suggests that the deposition of material into the void behind the tool causes a momentary reduction in forces required until the void has been filled. The efficiency of material deposition can therefore be inferred by the regularity and frequency of this oscillation in welding forces. [24] [27]

Onion rings must not be confused with flow band widths. Onion rings are dominated by the shoulder and only occur if there is transverse movement. There is still plastic material flow with spot welding, even though there is no onion ring formation. Onion rings are likely formed when excess plastic material escapes consolidation and is wiped by the shoulder behind the weld. An absence of onion rings in a weld means that not enough plastic material is being formed. Too much plastic material will form flash. The correlation between onion rings and flow band width ends there. There is no proof of a proportional relationship between onion ring width and flow band width.

3.12 Dynamic Recrystallized Zone Shape

At lower welding speeds, the shape of the weld zone tends to be basin shaped. At higher welding speeds the shape tends more towards a round or ellipsoidal shape. [28] This could signify the impact that the shoulder has on the weld beneath. At lower transverse speeds, the shoulder can deposit more energy into the weld, but the basin shape signifies that this depth is limited. At higher transverse speeds, this energy does not have as much time to deposit and the weld zone narrows.

This behavior of the weld zone seems to indicate that plasticization is due to viscosity of the material and not adiabatic shear bands. At higher rotation rates, shear rates are expected to increase, and shear band widths should increase. This relationship should not be affected much by translational velocity. This does not appear to be represented experimentally. It is more likely that an increase in temperature from an increase in heat generation at the shoulder is decreasing the viscosity of the material, allowing it to flow in the weld zone. At high transverse velocities, the shoulder heat generation does not have time to conduct in the z direction, resulting in an ellipsoid. At low transverse velocities, more heat generation can reach deeper into the weld, and the diameter of the weld nugget approaches the diameter of the tool shoulder.

3.13 Precipitate Depositing Effects

One last detail on material flow is the impact of precipitates on weld strength. It has been observed that at low transverse rates or to a lesser degree high rotation rates, coarse Mg_2Si precipitates tended to dominate the tensile fracture mode of AL 6061. This may be caused by high energy deposition values melting the material and allowing these precipitates to flow to the outside of the weld zone. This disruption in microstructure lead to lower yield strengths at the edge of the weld zone on the retreating side. [28]

4. Current Model

4.1 Modelling Summary

The purpose of discussing the progression of models for FSW in this thesis is not to delve deeply and develop another model. The purpose is to discuss all the conceptual models and unify concepts that appear to be experimentally proven to develop simple algebraic formulas based on the welding parameters that can predict steady state conditions during the weld. There are two large questions that define how the process of FSW occurs: Does heat generation occur through plastic dissipation or solely through frictional heating and can material flow be modeled as a solid or a liquid?

So far, this thesis has suggested that heat generation can occur as both friction and plastic dissipation, and that material flow can be modeled as both a solid and a liquid, depending on the welding parameters that create the welding thermo-mechanical environment. Therefore, this thesis will make assumptions for the optimal thermo-mechanical environment. This thesis assumes a sticking condition at tool interface, a heat generation model according to Equation 5, the material yields at a flow stress that can be calculated by Equation 13, and that material is deposited into the void through extrusion of high strain rate material on the advancing side and extrusion of lower strain rate material on the retreating side.

It is possible that the pin has a slipping condition for part of every revolution, or it may have several slipping revolutions before returning to a sticking condition. It is expected that the process is self-regulating to a degree. As the material is plasticized by high strain rates possible because of high pressure between the tool and the material, the material viscosity decreases and there is less pressure between the tool and the material. Additionally, when material is deposited into the void, this would also reduce the pressure between the tool and the material, leading to a slipping condition. Nevertheless, a return to a sticking condition is assumed because the sticking condition causes the dominant influence on temperature near the pin and is the dominant influence on material flow outside of extrusion.

The heat generation model may not be the most accurate model, but it is assumed that it is accurate enough to model heat deposition at steady state. The key concepts behind the model is that it assumes a sticking condition and that shoulder heat generation can be thought of as a preheating mechanism for the weld, and that the pin generates heat from plastic dissipation that dominates the temperature near the tool. This model can be used to determine if excess heat is being produced in the weld. If excess heat is produced, it is assumed that the material changes state, and can more accurately be represented as a liquid. This change of state will decrease resulting weld strength. The temperature, like the contact condition, is self-regulating, though. If excess heat is produced, the viscosity of the material decreases until the material flows, which decreases the plastic heat dissipation and the resulting temperature. This model assumes that the process self-regulates around the solidus temperature of AL 6061, 852K.

Adiabatic shear bands are not likely created during FSW. As already discussed, they require strain rates of 10,000 s^{-1}. Peak strain rates reported are between 1.7 and 1000 s^{-1}. [15] Even at the largest strain rate reported, adiabatic shear bands are not likely to occur, though the temperature compensated strain rates (Zener-Hollomon Parameter) is on the order of 1x10^9 from experimental calculations. Expected shapes of the weld zone at higher strain rates do not follow expectations of adiabatic shear band growth. There is a band of material that surrounds the pin and travels at the same velocity, but there is no evidence to support that this material was formed by the process of adiabatic shear banding.

The flow stress calculation in Equation 13 assumes that the machine is applying torque until the material yields, and that the flow stress can be inferred from this torque by assuming that 25% of the torque is from the pin. If the torque is not known, this thesis assumes that the temperature self-regulates around the solidus temperature. Some peak temperatures reported are reportedly at or higher than 98% the solidus temperature and support this hypothesis. [15] The flow stress is then calculated at just under the solidus temperature and the strain rate is iterated at different flow band widths and the result used to calculate viscosity until the viscosity converges to the critical viscosity. We can calculate the strain rate based on velocity of the material. Viscosity can then be solved for using Equation 10.

The strength of the weld is highly dependent on the weld's ability to deposit material into the void behind the pin. It is assumed that higher strength welds maintain a temperature below but near the solidus temperature. The material is frictionally heated until it flows, and enough plasticized material flows to fill the void behind the pin. If too much heat is deposited into the weld, this material becomes weaker due to a phase change in the plasticized material leading to lower strength welds. If enough heat is not deposited into the weld, not enough material plasticizes to fill the void behind the pin leading to tunnel defects.

4.2 Velocity Field Calculation

The material velocity equations used in this thesis are the same used by Nandan [4]. This model accounts for material recirculation and a range of tool slip values dependent on the rotational speed and distance from the pin. These equations also account for the possibility of Friction Stir Spot Welding (FSSW) in which a tool plunges but does not translate. The tool creates a "boundary layer" of unextruded material around the pin that does not require translation to form. Research has supported this idea of material recirculation. When welding two different alloys of aluminum together, it was discovered that initial material surrounding the pin remains near the pin for nearly the entire weld. [29] Equation 14 describes the velocity field used in this thesis in the radial and transverse directions respectively.

$$u_\theta = (1-\delta)(\omega\, r\, sin\theta - v\_t)$$
$$u_r = (1-\delta)(\omega\, r\, cos\theta)$$

Equation 14 - Material Velocity Near Pin

$$\delta = 1 - \exp(-\frac{\omega\, r}{\delta_0\, w_0\, r_s})$$

$v_t \equiv$ transverse velocity
$\mathrm{r} \equiv$ distance from pin axis
$\mathrm{r}_s \equiv$ radius of tool shoulder
$\omega \equiv$ rotational velocity
$\theta \equiv$ angle from direction of transverse motion
$\delta_0 = 0.4$
$\omega_0 = 50\, rad/s$

4.3 Strain Rate Tensor

The strain rate can be found from an estimate of the strain rate tensor. The strain rate tensor is found from an estimate of the velocity of material flow relative to the tool surface at the pin neglecting velocities in the z direction from Equation 14. Equation 15 and Equation 16 describe how the strain rate tensor and effective strain rate were calculated for this thesis. [4]

$$\varepsilon_{ij} = \frac{1}{2}\left(\frac{\partial u_i}{\partial x_j} + \frac{\partial u_j}{\partial x_i}\right), \varepsilon_{ij}\varepsilon_{ij} = \frac{\partial u_i}{\partial x_i}^2 + \frac{\partial u_j}{\partial x_j}^2 + \frac{1}{4}\left(\frac{\partial u_i}{\partial x_j} + \frac{\partial u_j}{\partial x_i}\right)^2$$

Equation 15 - Strain Rate Tensor

$$\dot{\varepsilon} = \sqrt{\frac{2}{3}\,\varepsilon_{ij}\varepsilon_{ij}}$$

Equation 16 - Effective Strain Rate

4.4 Critical Viscosity

Viscosity is calculated for a range of distances from the pin. Assuming that the material is sticking to the pin of the tool, the velocity of material at a given distance from the pin is calculated using Equation 14.. The velocity is then used to solve for the strain rate in Equation 16. The strain rate is used in Equation 12 and Equation 13 to find the flow stress at the location.

Finally, strain rate and flow stress are used to calculate viscosity in Equation 11. Viscosities above the critical viscosity of 5 MPa-s mean that the material is not flowing. Viscosities below the critical viscosity mean that the material is flowing.

4.5 Flow Band Width

The distance from the pin where the viscosity equals the critical viscosity for AL 6061-T6 equals the flow band width for the given welding parameters. Increasing rotation rate appears to increase flow band width to an optimal value and then start to decrease at rotation rates over 1400 RPM. Figure 4 and Figure 5 demonstrate the calculated flow band width’s relationship to rotation rate and traverse rate respectively. These figures represent calculated flow band width using data from Lim et al.

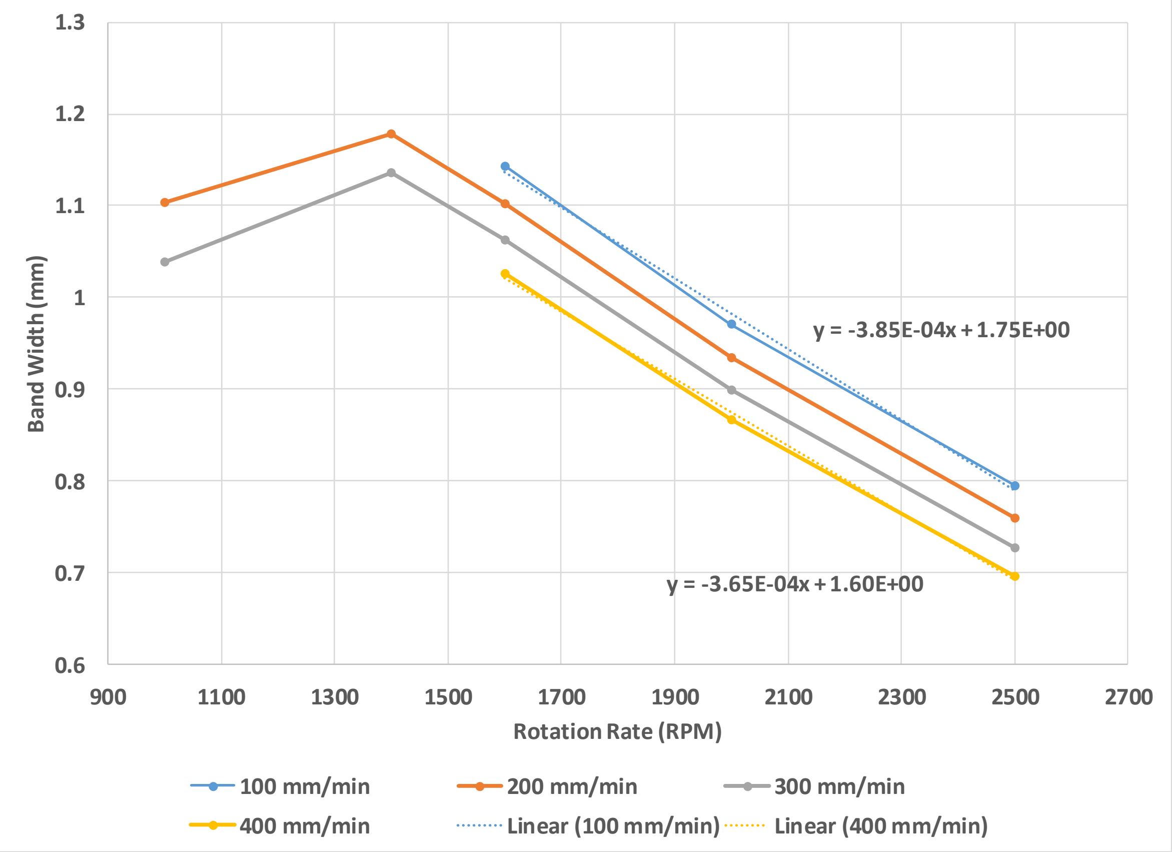

Figure 4 - Flow Band Width vs Rotation Rate

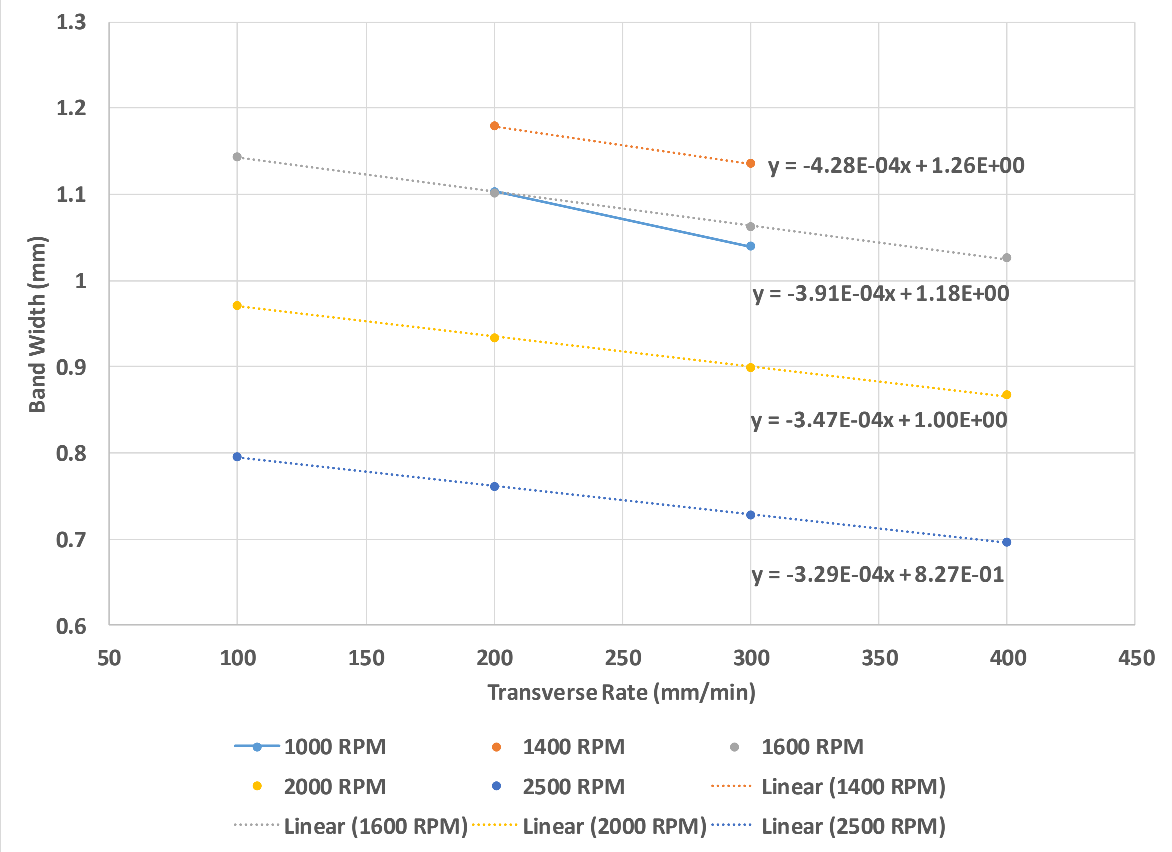

Figure 5 - Flow Band Width vs Transverse Rate

5. Weld Parameter Mapping

5.1 Current Weld Parameter Metric

Weld Parameter maps are a useful method to help understand the friction stir welding process. The figures given in the paper from Pei and Dong describe how welding parameters affect weld quality. [20] The mapping of successful welds is based on physical models, and these insights can be used to describe how tool features may affect the weld process. The experimental data was taken from Lim et al. [28] and Trueba et al. [30]. A contour map of the welds was created that describes the yield strength of the welds is shown in Figure 6.

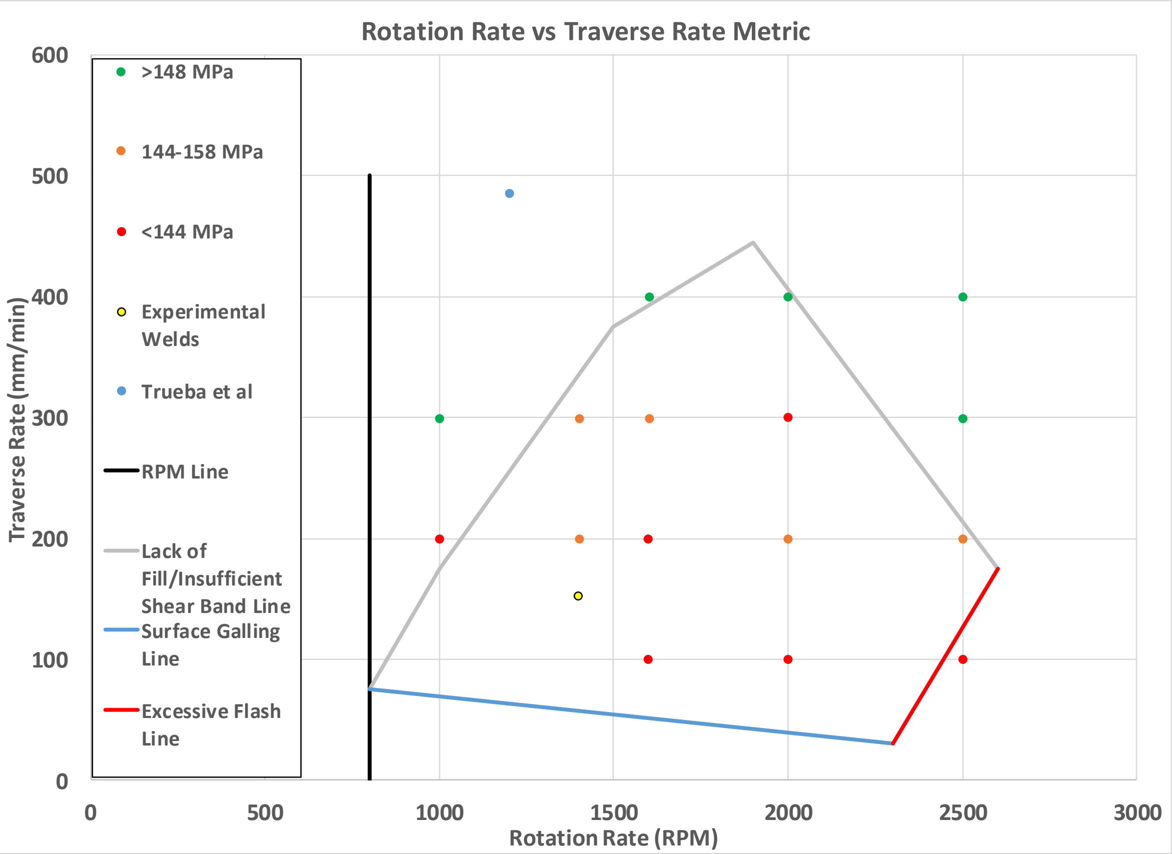

Figure 6 - Pei and Dong Welding Parameter Metric

The first boundary provides a minimum rotation rate, below which a sufficient temperature cannot be sustained through heat generation from plastic dissipation work because the plastic strain rate is too low. For AL6061, the rotation rate should be at least 800 RPM and the features considered in this thesis do not affect the limit meaningfully. [20]

The second boundary sets the upper limit of rotation speed dependent on traverse rate. Above this boundary at lower rotation speeds, defects due to insufficient plastic flow and voids located in the advancing side of the stir zone occur. [31] Scrolling on tool shoulders may increase temperature near the pin so that the width of the shear band increase which allows increased plastic flow at lower rotation rates and the material stays plastic long enough to be consolidated into the void behind the pin. Threaded pins also cause material flow in the Z direction which increases strain on the material and may also increase the width of the shear band. [20] Above this boundary at higher rotation speeds causes defects from abnormal stirring. High rotational speeds cause non-uniform velocity fields and as a result thinner shear bands that do not allow enough plastic material flow into the void behind the pin. These void formations are more likely at the advancing side of the stir zone. [20]

The third boundary sets a lower limit for traverse rate. Below this boundary, the contact pressure between the pin and the material is too low. The resulting friction is not enough to cause the material to “stick” to the pin and cause the material to plasticize due to a high strain rate. The friction still causes heat, but a shear band is not formed and defects from “surface galling” or tearing of metal at the top of the weld occur. [20] [31] Threads provide more surface area to induce the material to stick to the pin, and it also may increase strain by inducing vertical material flow.

The final boundary sets an upper limit on rotation speed above which excessive surface flash is predicted. Surface flash happens when the weld temperature approaches the material solidus temperature because too much energy has been deposited into the weld. This is often caused by too much axial force in the Z direction. [20] It has been shown that increasing traverse rate can decrease the required axial load [32], but the amount that the traverse rate can be increased is limited by the strength of the tool used. Shoulder scrolls may increase frictional temperature and contribute to excessive flash occurring at lower rotational speeds.

5.2 Proposed Weld Parameter Metric

While this is a useful tool to compare different welds, it neglects the possibility of different shoulder and pin sizes from different tools. This allows the possibility that two separate welds with the same welding parameters could have drastically different results. A better way to characterize welding parameters would be something that directly compares the thermal model to the material model. While this method would couple the effects of changes in welding parameters, it is not as straight forward. Its utility more than makes up for this weakness.

A proposed weld parameter matrix compares heat generation and flow band width. The heat generation considers tool dimensions as well as rotation and transverse rates. Equation 5 is used for the heat generation and assumes a sticking condition at the pin. The method described in section 4 is used to find the flow band width. The proposed metric is shown in Figure 7.

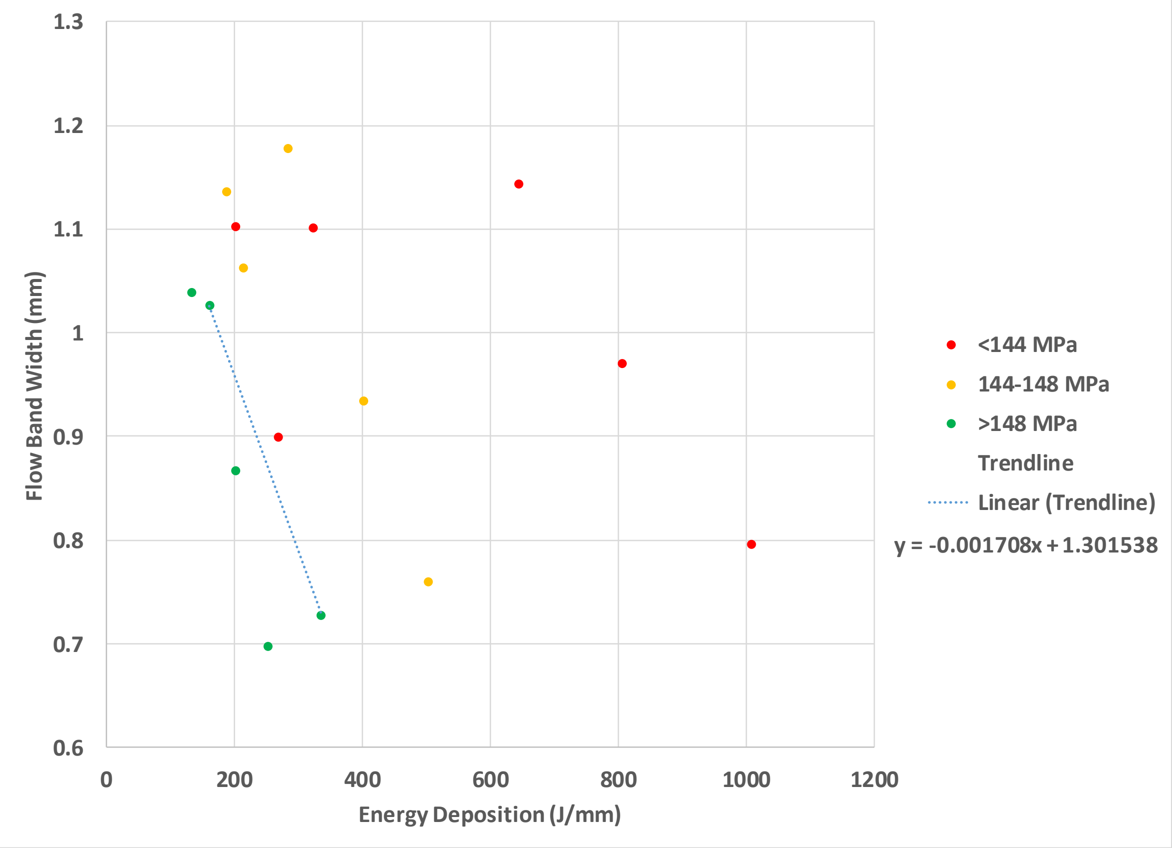

Figure 7 - New Welding Parameter Map

As can be seen, there is a clear area where high strength welds appear. Furthermore, there seems to be a trend that larger flow bands allow lower energy deposition, while smaller flow bands tolerate more energy deposition. Figure 8 illustrates this trend by plotting the energy deposition versus strength for groups of welds with the same shear band width. There are strong relationships within the same shear band grouping between energy deposition and strength.

For welds with higher energy depositions, the material may experience melting, in which case a different, non-solid-state joining phenomenon may be occurring. The process is still self-regulating around a certain set of thermo-mechanical conditions, it is a question of where the process is self-regulating from. Most models consider the material approaching a plastic state from a solid state. The temperature is increased through both frictional and plastic dissipation until the solidus temperature is reached, and viscosity decreases until material flows and pressures on the material are released and the process repeats.

The process can also approach a plastic state from a liquid state, though. The plastic material closest to the pin can begin to melt while plastic material towards the outside of the flow band remains in a visco-plastic state. The melting of the material decreases the density and resulting pressures resulting in an increase in the slip rate of the tool. The temperature then falls to the solidus temperature because the temperature of material near the pin is dominated by plastic dissipation and there is no plastic dissipation if slipping is dominant. Once the material returns to a plastic state, a sticking condition occurs again and the process repeats. Higher temperatures mean more phase changes and a lower weld strength if this micro-melting process is occurring.

Crawford noted that a Couette Flow model correlated better than a visco-plastic flow model weld pitches greater than 210 revolutions per inch. [2] This corresponds to about 8.33 revolutions per millimeter. Like before, this does not consider the dimensions of the tool and is not a physical explanation. A weld pitch of about 8.33 revolutions per minute for his tool corresponds to an energy deposition of about 750 Joules per millimeter using the tool dimensions in Crawford's experiment. Interestingly, this energy deposition limit is also present in traditional arc welding when comparing arc length to weld width. It is explained in arc welding as the limit where higher arc length increases heat distribution without significantly altering heat input. [3] This phenomenon appears to occur at around 400 Joules per millimeter in the data given by Lim et al. If the flow band graphs are then split into energy depositions roughly below and above 400 Joules per millimeter, precise relationships start to appear. These relationships are shown in Figure 8.

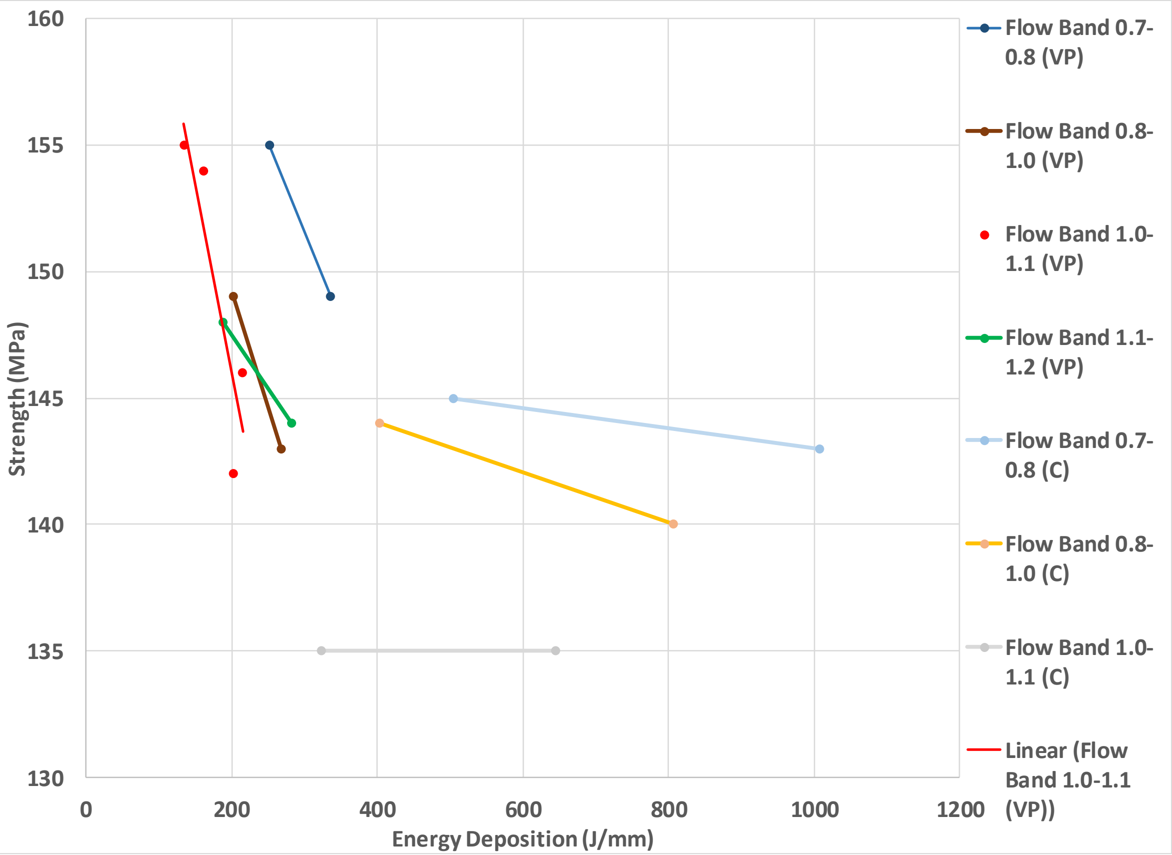

Figure 8 - Energy Deposition vs Strength

So far, we have discussed optimal welding parameters and an upper limit on energy deposition for a given flow band width. From the earlier discussion of flow bands, a lower limit on energy deposition can be given below which flow bands will not form. This limit will be different for every tool and welding set up but will be dependent on lowering viscosity below the critical viscosity.

Using the experimental welding parameters, a yield strength of approximately 140 MPa with no defects is predicted by first metric. It is relatively difficult to make this interpolation given the metric. The proposed metric can give an equation for predicting strength. Since the experimental welds in this thesis deposit much more than 750 J/mm, it is well within the Couette Flow Model zone. Using calculations that will be developed in section 9.1 to verify the viscosity model, the estimated flow band width is about 5 millimeters. Estimating a strength for Couette

Flow using an energy deposition of 2231 J/mm and a flow band width of 5 mm, the predicted strength is lower than 135 MPa. The line is projected using only two data points, and such a drastic energy deposition suggests the actual strength will be lower. More importantly, it provides an intuitive way to evaluate how tool features could affect weld quality in the scope of the models given above.

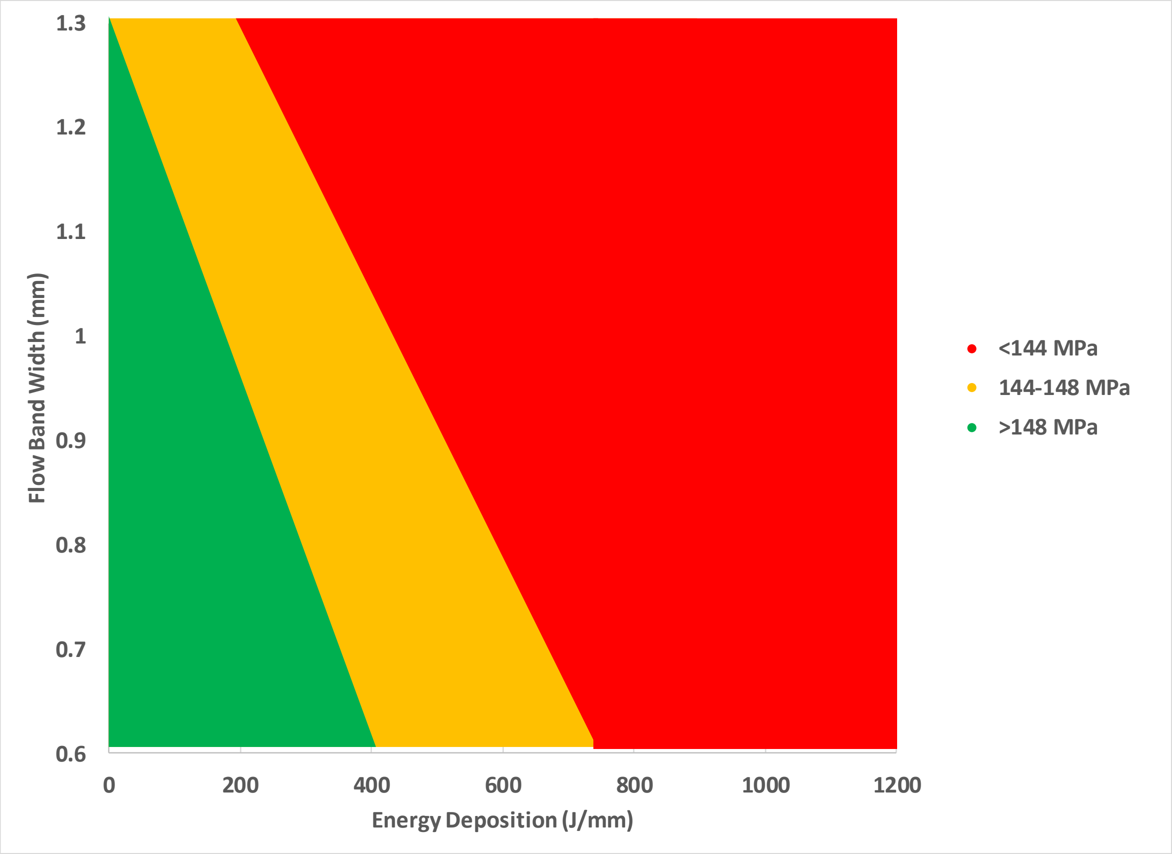

Figure 9 - Generalized Welding Parameter Map

6. Tool Components

6.1 Shoulder

The shoulder generates frictional heat that is distributed into the weld and acts as a preheating mechanism. It also contains plasticized material from the pin and consolidates it into the weld. Shoulder diameter is typically three times the diameter of the pin. [5]

Early shoulder designs were concave that trapped escaping plasticized material until it can be deposited into the void behind the weld. These tools required the tool to be tilted to allow material into the concave shoulder shape. This required load to be applied in directions both perpendicular and parallel to the weld direction to keep the tool from rising out of the material. This requirement also limited the transverse speed. Finally, the tool tilt angle causes material flow out of the material resulting in excess flash. [33]

The first attempts to make a convex shoulder were made by TWI, but they were unsuccessful because the convex shape pushed material away from the welding zone. Scrolls were eventually introduced and fixed this problem. Convex shoulders did not require a lead angle because the outer edge of the shoulder did not contact the material allowing for rapid changes in weld direction. It also provides more flexibility in weld height changes, so that the amount of shoulder engagement does not affect weld quality as much and allowed for control by varying shoulder engagement.

6.2 Pin

Pin heat generation is dominated by plastic dissipation and affects peak temperature near the pin more than the distributed frictional heat generation by the shoulder. [5] Typical pin diameters are the same as the thickness of plates to be welded. [5] The pin deforms and shears material at the faying surfaces of the welded materials and the large strain rates, strains, and heat generation plasticize the materials. Concurrently, the pin transports the material around the tool and deposits it in the void. [33] This material is extruded between the pin and the parent material on the retreating side. On the advancing side, the material can become entrained in a rotation zone like a boundary layer and eventually flows into the void behind the pin in arc-shaped features. [25]

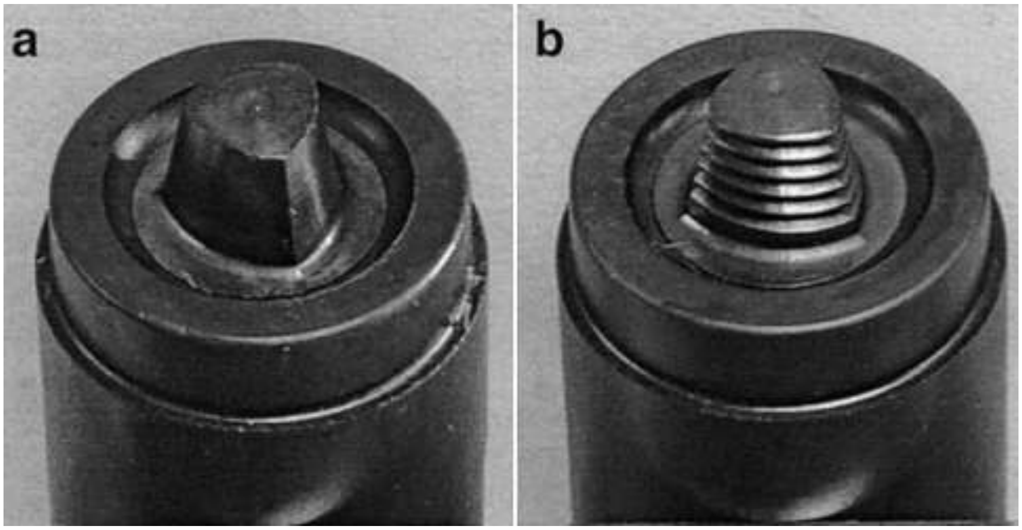

Figure 10 - TWI Trivex tool (a) and MX-Trivex tool (b)

The most common shape for pins is a flat-bottom cylindrical pin because it is easy to machine. Round-bottom pins can reduce tool wear upon plunging and improve the weld root quality but are harder to machine. Truncated-cone pins have lower transverse loads and can be used to weld thicker plates at faster speeds. Where threads are not possible in high-temperature materials like ceramics, a stepped spiral profile can be used. TWI has developed a Whorl pin, the Triflute pin, and the Trivex pin. The Whorl pin has a helical ridge on the pin surface like an auger that directs material flow downward. This pin reduces the displacement volume by 60% and reduces traverse loads. The Triflute pin contains three flutes cut into the helical ridge of the Whorl and further reduces the displacement volume of the pin by 70% over the Whorl. The Trivex pin has a triangular shape and reduced traverse forces by 18-25% and normal forces by

12% over the Triflute pin. [34] [35]

6.3 Material

The material of the pin can affect welding parameters in several minor ways. The material of the tool must withstand maximum forces at welding temperatures. For welding at lower temperatures, like the welds considered in this thesis, H-13 tool steel, Ferro-TiC SK, and MP-159 can be used with maximum working temperatures around 550 degrees Celsius. For higher temperature welds of steel or similar metals, Rhenium, Tungsten, and Polycrystalline Cubic Boron Nitride tools are often considered because of their maximum work temperatures of almost 2000 degrees Celsius. [2] [36]

7. Tool Component Features

7.1 Shoulder Scrolls

Shoulder scrolls pushed plasticized material from the outside of the shoulder back towards the pin. This allows flat or convex tools to be used at reduced welding forces and increase traverse speed without pushing all the material away from the weld zone or needing to operate with a tool angle. [30] Scrolls also allow material displaced by the probe to escape without being displaced as flash by directing it back toward the pin where it can eventually be deposited back into the void left by the pin. [6] Shoulder scrolls also allow flat shoulders to be used over concave shoulders and reduce welding forces required and increase traverse speed.

Scrolls have two suspected effects on material with respect to weld parameters. Scrolls may increase the friction coefficient and resulting energy deposition. If there is no evidence of a higher friction coefficient, this may suggest that a sticking condition occurs at the shoulder's surface. If there is a significant difference in weld strength between scrolled and non-scrolled tools, this would confirm theories that scrolls improve material flow toward the pin and prevent material from being pushed away.

7.2 Pin Threads

The main function of threads is to induce vertical material flow. [37] [2] [25] Threads do not affect maximum temperature or temperature contours. [38] The threads are rotated in a direction that drives material downward. As the material reaches the bottom of the material, it is then forced away from the pin and then starts movement back upward toward the shoulder. This induced vortex moves hot material away from the shoulder and may prevent material on top from receiving too much energy. [12] [25] It also increases strain rate and strain on the material near the pin, which may increase flow band width. This vortex may improve material flow to the root of the weld, decreasing the likelihood of root or tunnel defects. It has also been observed that the addition of threads reduces traverse forces. [2]

Threads may help decrease energy deposition for a set of welding parameters by transporting hot material near the heat generation caused by the shoulder down into cooler material. Weld strengths indicative of lower energy deposition would confirm this hypothesis. It has also been suggested that increased material flow from threads can increase the strain rate and the flow band width. Weld strengths proportional to flow bands widths could confirm this hypothesis.

7.3 Triangular Pin

It was predicted that lower ratios between tool area and swept area would lead to lower traverse force at a modest increase in required torque. The triangular pin required lower traverse and axial forces. Interestingly, the threaded triangular pin required more traverse forces. [34] [35] Triangular shaped pins may provide pockets for plasticized material to be regularly distributed into the void behind the pin as the tool rotates. Since they are depositing plasticized material three times per revolution as compared to once per revolution for circular pins, they are maintaining a lower average pressure on the tool. This may account for lower traverse forces.

The triangular pin tool will be compared to the other tools in terms of weld strength, traverse forces, and axial forces. Higher strength welds would suggest that material flow is improved using triangular pins. The claims of decreased axial and traverse forces will be verified or rejected.

8. Experimental Configuration

8.1 Machine Setup

Welds in this thesis were conducted at the Vanderbilt University Welding Automation Laboratory with a Milwaukee #2K Universal Milling Machine that has been retrofitted with motors and instrumentation to control spindle speed, transverse speed, lateral speed, and vertical position. A Kistler dynamometer measures forces in x, y, and z directions, and torque. The sensors and motors are connected to a Dell Precision 340 that uses MATLAB's Simulink Real-Time to generate a control signal that interfaces with a real-time target. The VUWAL FSW set up is pictured in Figure 11.

Three butt welds of aluminum 6061-T6 were performed with each tool at a rotation rate of 1400 RPM and a traverse rate of 152.4 mm/min. Plunge depths were iterated until approximately 80% of the shoulder maintained engagement in the material. These values were in the range of 5.4102 to 5.461 millimeters. The dimensions of the plates were approximately 406.4 x 76.2 x 6.35 millimeters. The nominal composition of aluminum 6061 is 1.0% Mg, 0.6% Si, 0.3% Cu, and 0.2% Cr.

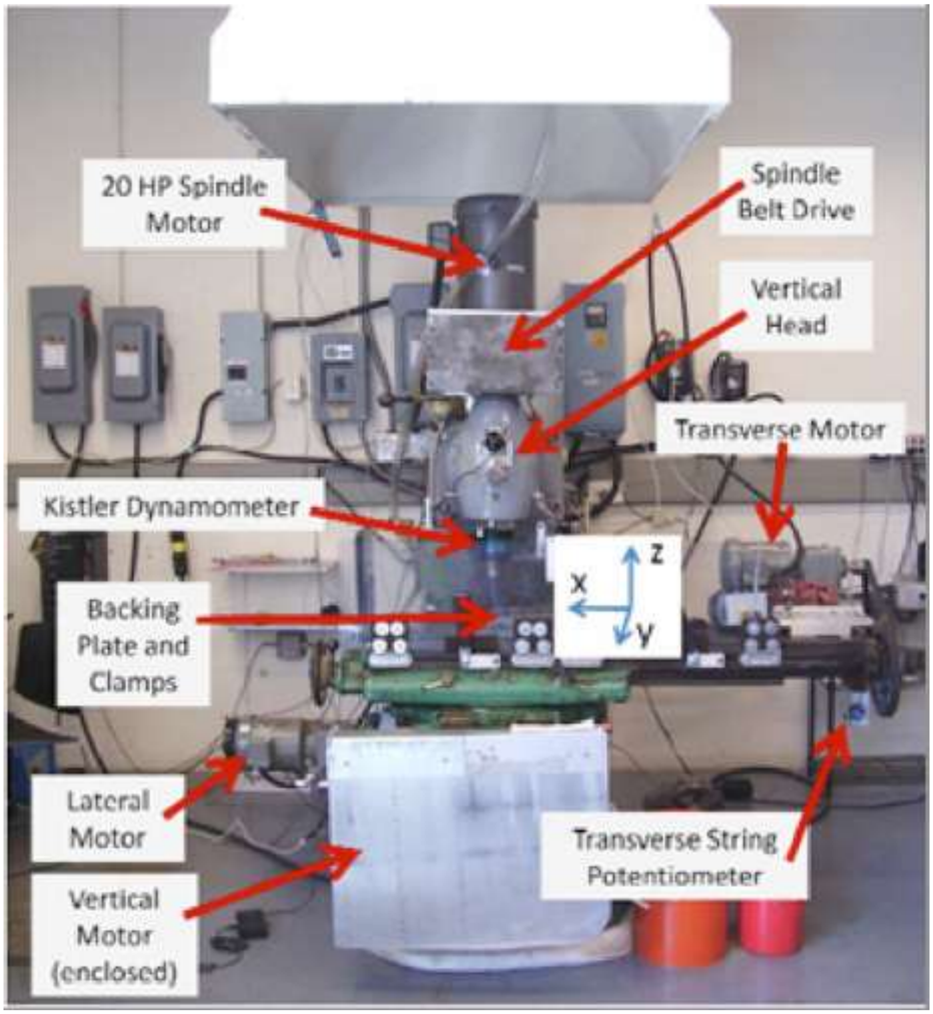

Figure 11 - VUWAL FSW Machine [32]

8.2 Anvil Topography

This project began when it was noticed that weld quality during the second half of welds was poor. Specifically, excessive flash increased as the weld progressed, and the tool was taking too much material from the advancing side. Original hypotheses for the origin of these defects were a loose or misaligned tool causing it to wobble, or the topography of our anvil was no longer flat causing the tool to engage more material as the weld progressed.

To rule out a misaligned tool, the angle of the tool in relation to the anvil was examined using levels and image processing . No misalignment was found. To examine the existence of a tool wobble, a high-speed camera was used to record several welds looking down the traverse axis. An image processing program was written to identify the tool from background noise, and then track the position of the top and bottom of the tool. From this information, an angle was determined and tracked throughout a weld. The max deflection of the tool was found to be about 0.5 degrees with a dominant frequency of 24.78 Hz. The tool was rotating at 1400 RPM, or 23.33 Hz. This was deemed most likely too small to affect weld quality.

Next, the topography of both the anvil and the specimen clamped onto the anvil were mapped by lowering the tool until an axial force was detected by the dynamometer. The height was recorded at various locations on the anvil alone and with specimen until a topography could be interpolated. The topography of the anvil is shown in Figure 12.

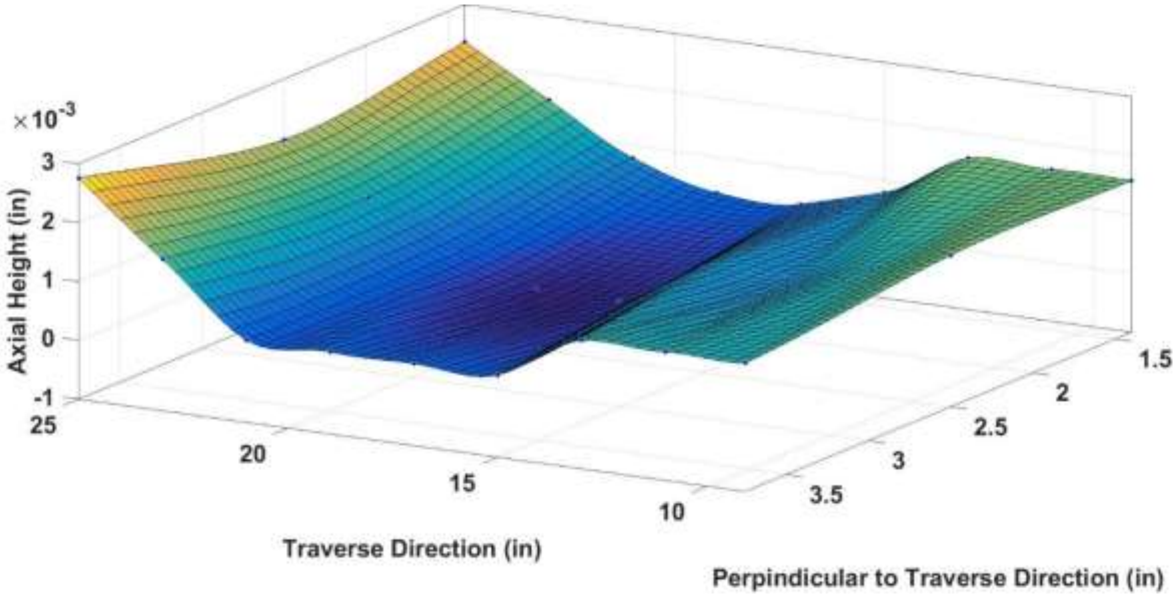

Figure 12 - Anvil Topography

8.3 Specimen Topography

Next, the topography of the specimen clamped onto the anvil was mapped using the same methods used to find the topography of the anvil. The specimen topography is shown in Figure 13.

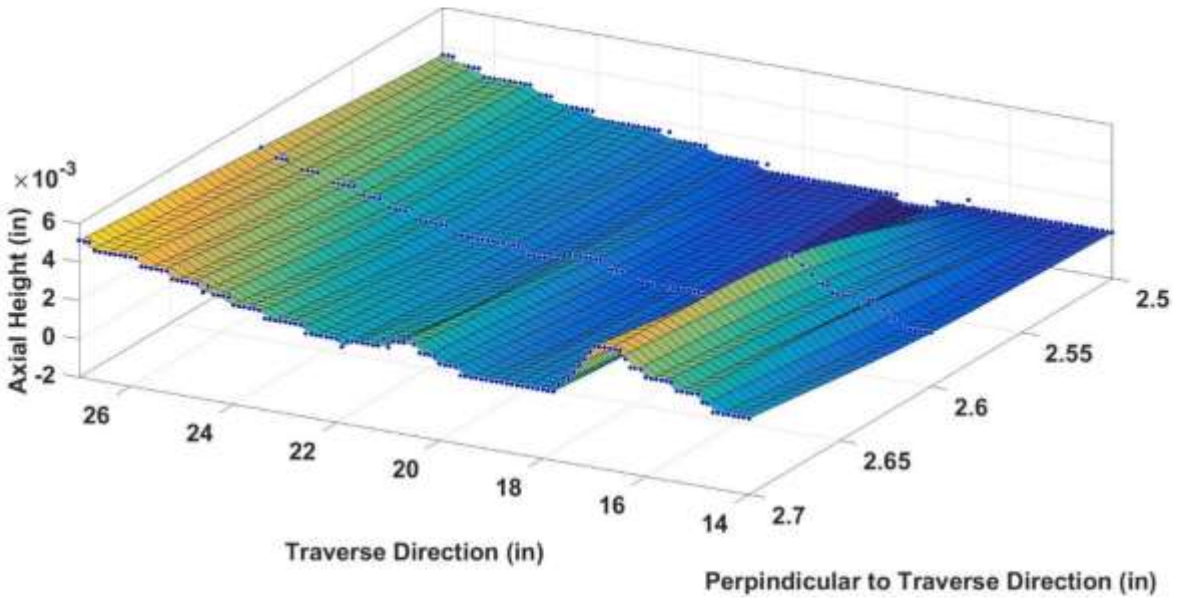

Figure 13 - Specimen Topography

There is an obvious low spot on our anvil that translates to the specimen when it is clamped to the anvil. This spot was most likely caused over years of FSW plunges all at approximately the same location. It was estimated from past experimental observations that a height change of around 0.005 inches could affect weld quality. The difference in height on the specimen from the lowest point to the highest point is 0.0051 inches. While this difference could start affecting welds, it should only affect welds at the highest point, or the extreme end of the weld, and then only slightly. Excessive flash in previous welds began to become a problem around halfway through the weld, or at about 20 inches in the traverse direction on the figure. To rule out weld topography, a weld in the opposite direction was conducted. Severe flash was still reported, though it was noticed earlier in the weld.

8.4 Tools

Four different tool designs were used in this thesis. All tools were manufactured of H-13 steel heat treated to Rc 48-50, had one inch (25.4mm) diameters, shoulder angles of 7 degrees, 0.25 inch (6.35 mm) pin diameters, and 0.185 inch (4.699 mm) pin height. The first tool had a round, threaded pin and a scrolled shoulder. The second pin had a round, threaded pin but no scrolled shoulder. The third pin had a scrolled shoulder but no threads on the circular pin. The final tool had a threaded pin, scrolled shoulder, and a triangular shaped pin. The tools are pictured in Figure 14 from left to right: TPS 9545, TP 9545, PS 9545, TPS 9545_t.

Figure 14 - Tools used in experiments (TPS 9545, TP 9545, PS 9545, TPS 9545_t)

8.5 Weld Data

A Kistler Rotating quartz four-Component Dynamometer (RCD) measured forces and torque on the tool. The output voltages of the dynamometer were digitized and transmitted to a stator connected to a computer. The stator was rigidly, concentrically mounted 2 mm away from the RCD.

A custom C# package is used for data collection. This package records the output data from the dynamometer and outputs a CSV text file. This data is then imported into MATLAB for post processing.

8.6 Optical Testing Methods

Several optical methods were attempted in analyzing and testing the welds. Videos were taken of some welds to measure shoulder engagement. Since the diameter of the tool is known, the image can be processed to determine the width of the shoulder in contact with the material. This is a potentially easy method to control for changes in the topography of the weld or thermal expansion of the material, but vibrations made calculations difficult. If the camera can be reliably dampened, this may be a way to control the shoulder engagement without knowledge of the system.

Optical methods were also used to more precisely measure distances. By using a reference length in photos of the dynamic recrystallized zone, pixels were related to distances and precise widths of flow bands could be measured. This was especially useful when the recrystallized zone was difficult to see, but post processing of the image could increase contrast between the recrystallized zone, heat affected zone, and parent material.

8.7 Tension Testing Methods

Welds were tested in an Instron Tensile Testing machine. Five specimens were removed from each weld, 60 specimens in all. A sample showing where tensile test specimens were taken is shown in Figure 15. Three of the five specimen were perpendicular to the weld and spaced along the weld. The remaining two were parallel with the weld and were in the weld zone. Only tests perpendicular to the weld are included in the results, as all the parallel samples failed in the Instron machine’s grips.

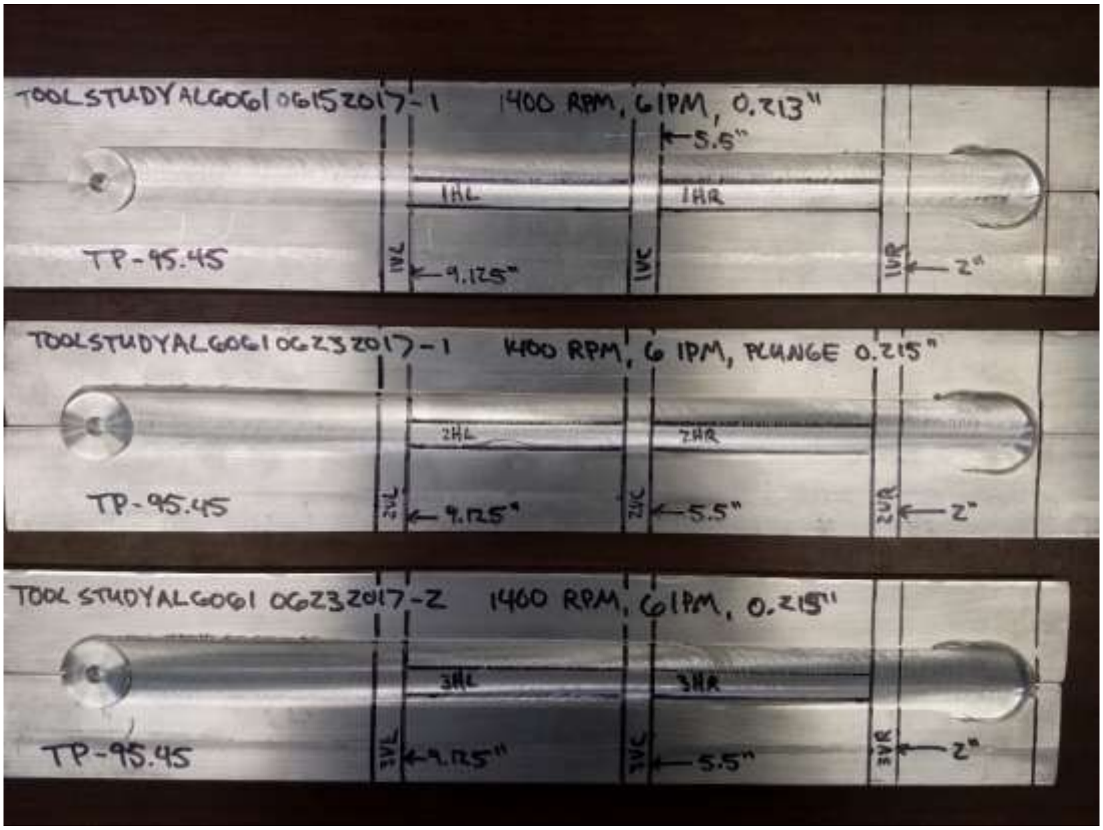

Figure 15 - Sample showing locations of tensile test specimen

9. Results

9.1 Flow Band Model Verification

To the author’s knowledge, there has never been a test of the critical viscosity theory proposed by Nandan et al. To verify the Nandan model, three welds were completed with rotation rates ranging from 1200 to 1600 RPM and a fixed transverse rate of 254 mm/min, and three welds were completed with a fixed rotation rate of 1400 RPM and transverse rates ranging from 101.6 to 203.2 mm/min. Table 1 summarizes the weld parameters and resulting flow band widths for the verification welds.

Table 1 - Verification Weld Parameters and Results

Name	Rotation Rate (RPM)	Transverse Rate (mm/min)	Measured Flow Band Width (mm)	Predicted Flow Band Width (mm)	Error
Verification Weld 1	1200	254	4.23	4.79	13.13%
Verification Weld 2	1400	254	4.34	4.62	6.37%
Verification Weld 3	1600	254	4.37	4.45	1.83%
Verification Weld 4	1400	101.6	5.31	5.20	2.10%
Verification Weld 5	1400	152.4	4.94	4.99	1.04%
Verification Weld 6	1400	203.2	4.72	4.79	1.49%

The pin was stopped and quenched after steady state conditions were met. Specimens were then taken just behind the keyhole left by the pin in the material. These specimens were water-sanded, polished, and etched with Kellers reagent. The resulting etch of the weld was analyzed to determine the width of the flow band. The measured flow band width was found by measuring the width of the recrystallized zone caused by the pin through the center of the area (shown by white arrows on images). The thickness of the specimen is known to be 6.35 mm and is used as a reference distance to convert the pixel width to a width in millimeters. The resulting width in millimeters is then divided by two because the flow band is theoretically symmetrically created on both sides of the pin. The etches of the six verification welds filtered using MATLAB’s ADAPTHISTEQ filter are shown in Figure 16.

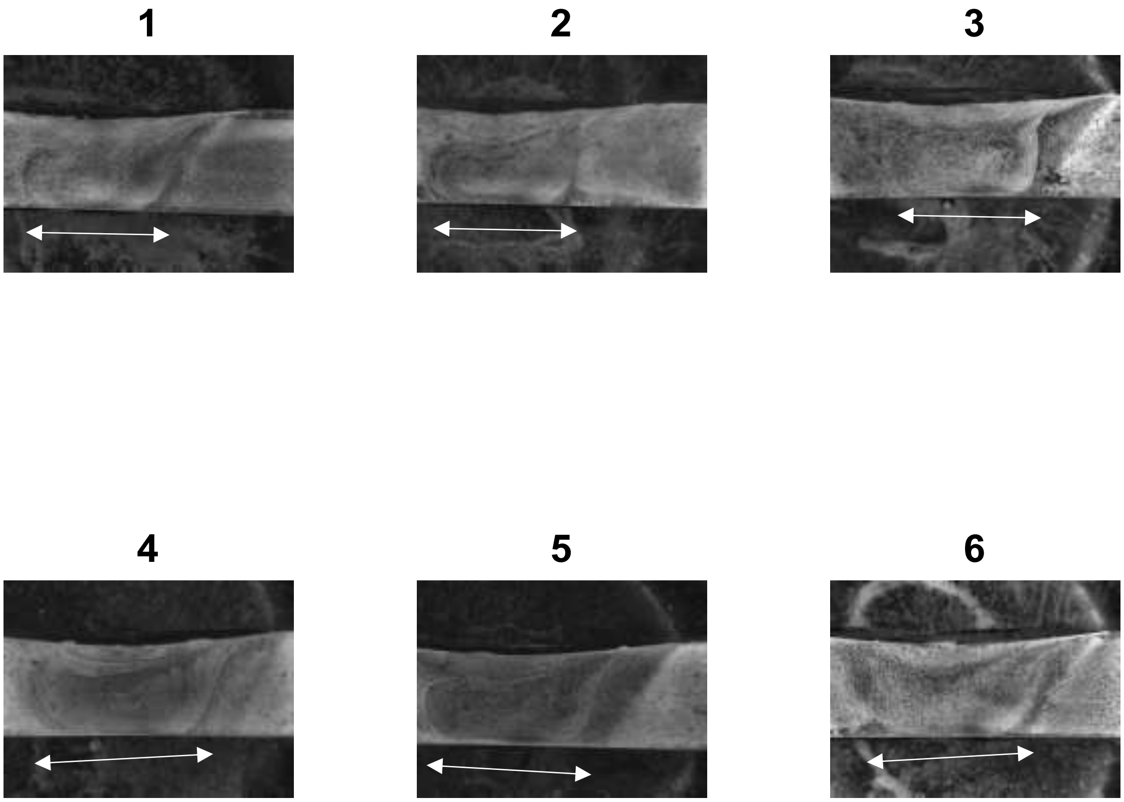

Figure 16 - Verification Weld Etches

One trend identified from these images is the relationship between rotation rate and the angle of the recrystallized zone due to the pin on the retreating side of the weld. As rotation rate increases from 1200 RPM in Weld 1 to 1600 RPM in Weld 2, the angle starts near 45 degrees and approaches vertical. This trend seems to be dependent on rotation rate and not energy deposition because there is no noticeable change in the angle among welds with similar energy depositions such as welds 4 to 6.

Predictions for flow band width were calculated using the methodology described in Chapter 4. The temperature was assumed constant at the solidus temperature at the interface between the pin and the material and the Rosenthal equations were used to model the temperature radially from the interface. Strain rate and flow stress were calculated at all distances using the Zener-Hollomon method. These values were used to calculate viscosity at a range of distances from the pin until the critical viscosity was exceeded. The results are summarized in Table 1.

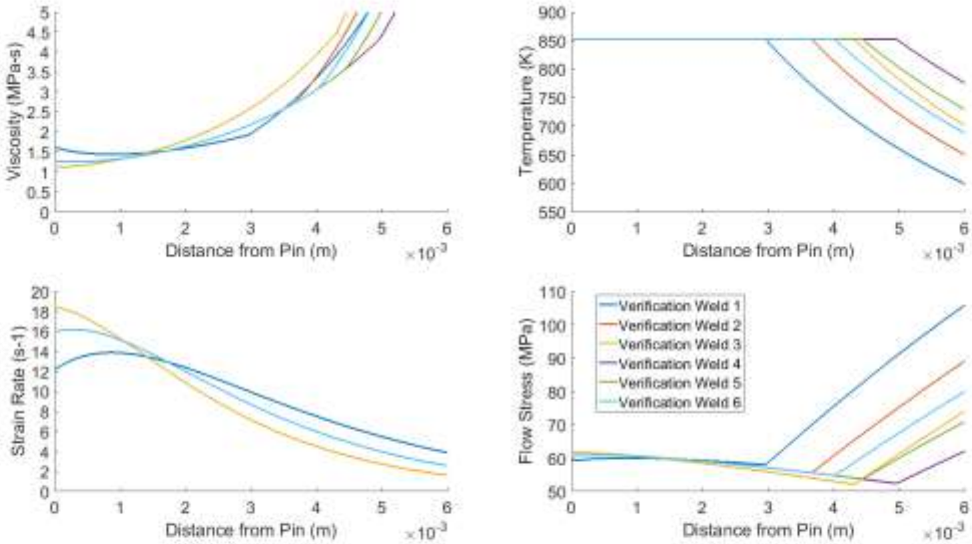

Figure 17 - Flow Band Width Calculations

The resulting flow band width model dependent on critical viscosity is highly dependent on energy deposition. Figure 20 demonstrates this relationship. The three tightly grouped data points in the lower left section of the graph have a fixed transverse rate, and rotation rates ranging from 1200 to 1600 RPM. The three data points that are more dispersed have fixed rotation rates with traverse rates ranging from roughly 100 to 200 mm/min. There are not enough data points to make any firm observations, but it appears that higher rotation rates will eventually result in less increase in flow band widths but reducing traverse rates will linearly increase the flow band width. The energy deposition is dependent on the tool dimensions, rotation rate, and transverse rate. The relationship for both the rotation rate and the transverse rate with the flow band width is described in Figure 19 and Figure 20. Linear relationships with slopes similar to the trendlines shown but with shifted y-intercepts are predicted for data where only one data point is shown.

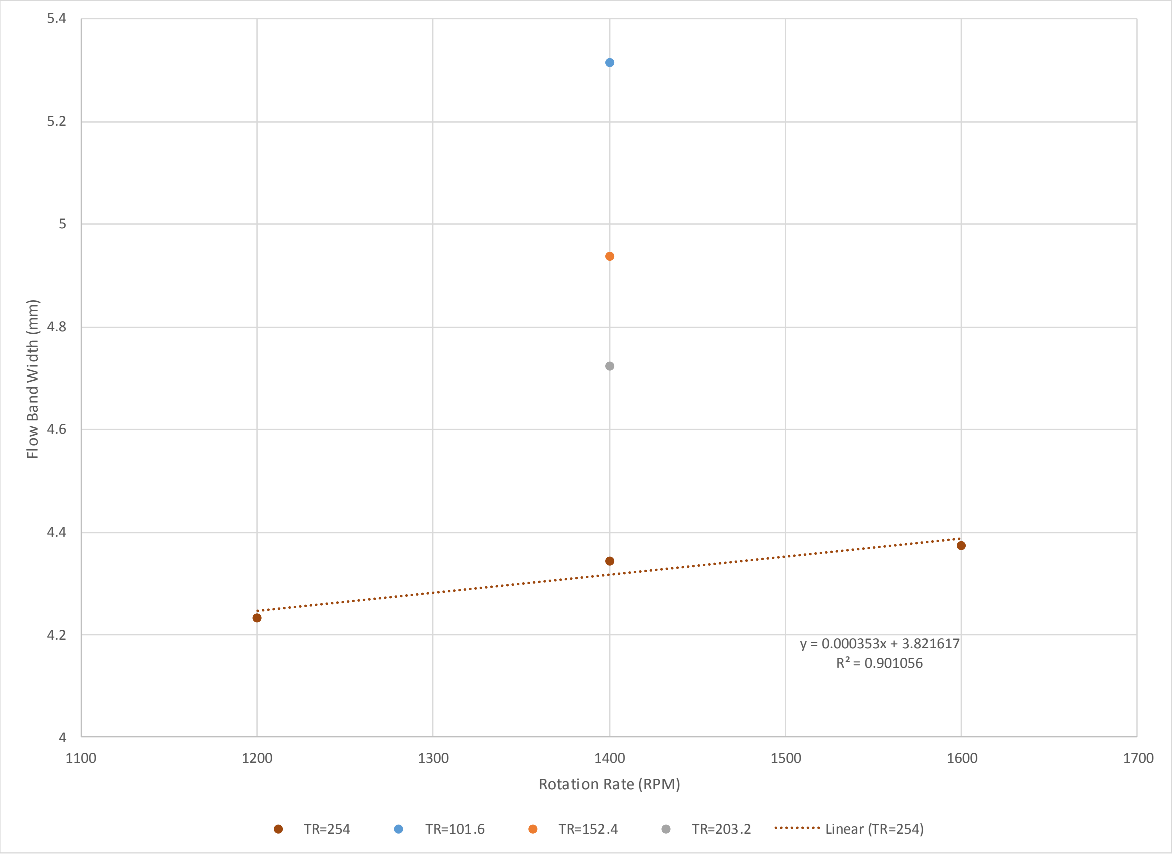

Figure 18 - Verification Welds Rotation Rate vs Flow Band Width

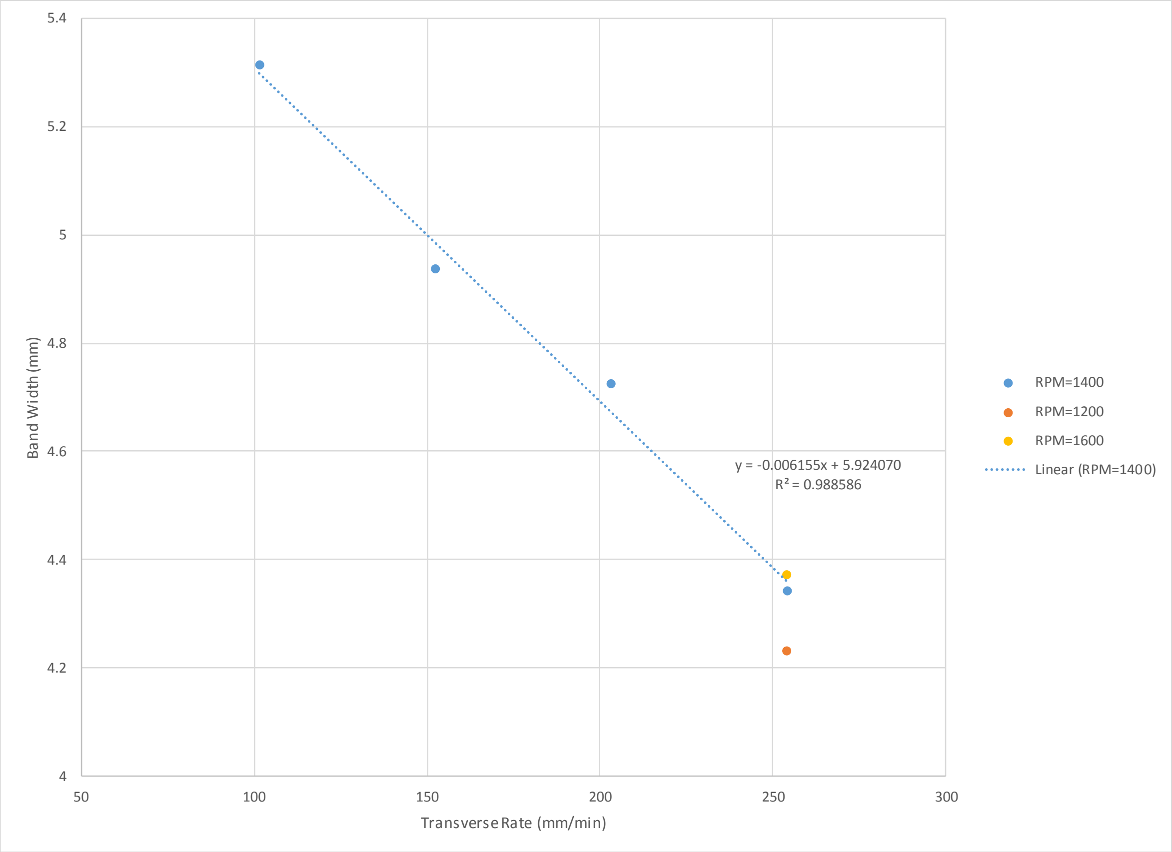

Figure 19 - Verification Welds Rotation Rate vs Flow Band Width

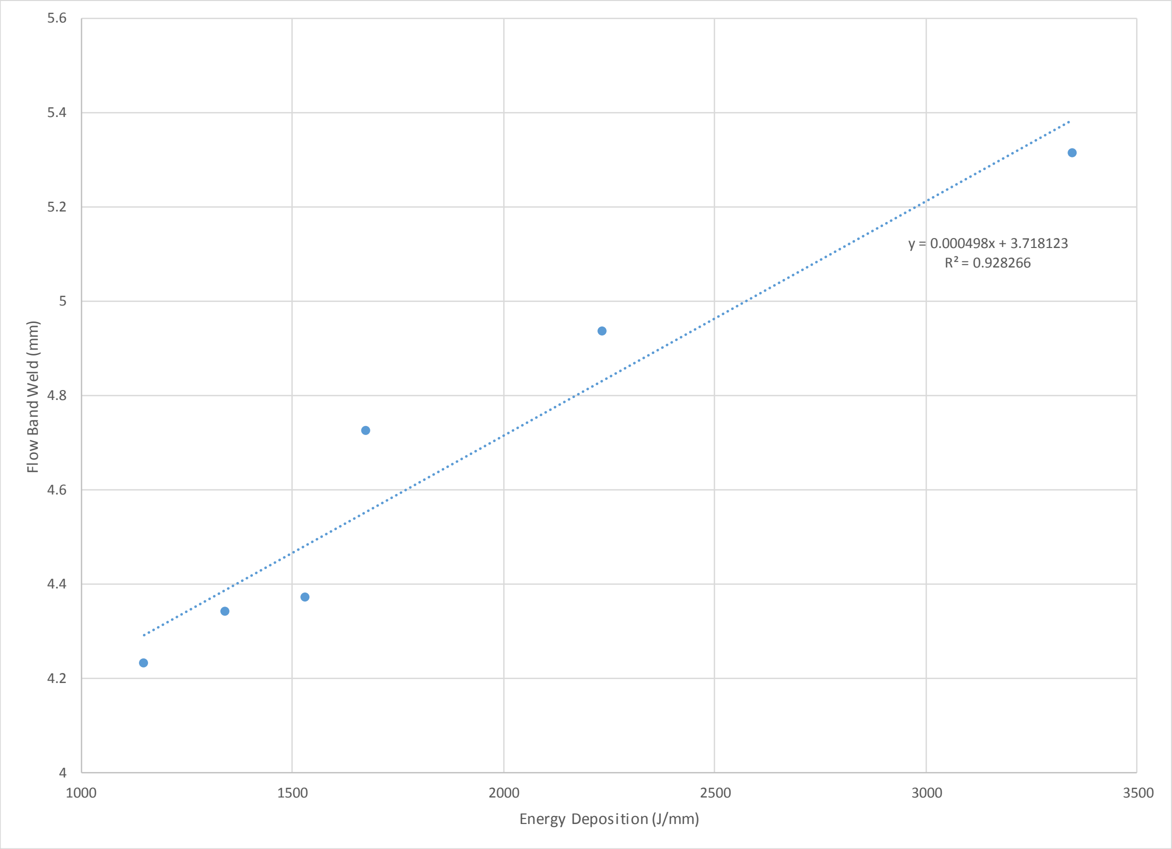

Figure 20 - Energy Deposition vs Flow Band Width

Error between predicted flow band widths and measured flow band widths for verification welds ranged from 1% to 13%. Error was discovered to be largely influenced by the weld's energy deposition. Lower energy depositions resulted in higher error for the prediction. This error split is between welds with more or less than 1600 J/mm energy deposition and is depicted graphically in Figure 21.

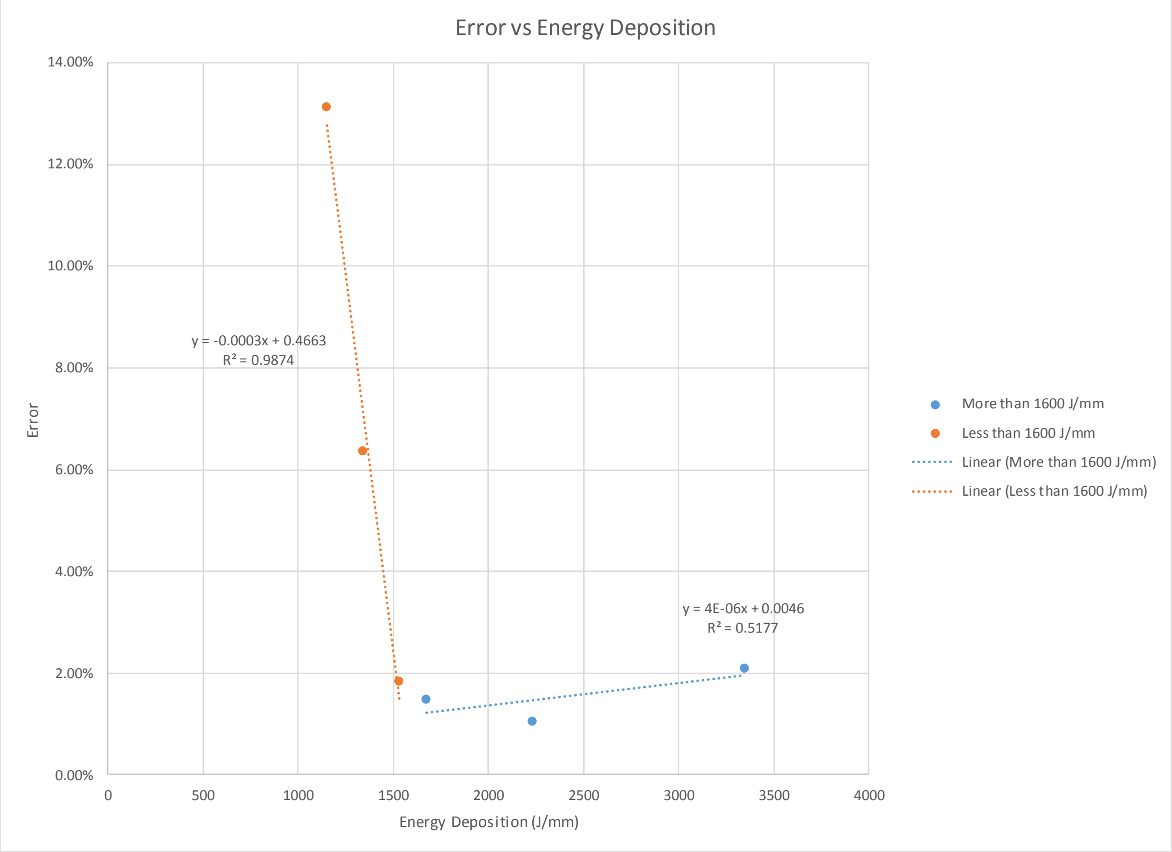

Figure 21 - Flow Band Prediction Error vs Energy Deposition

Etches were also made of specimens from welds using the tools TP 95.45, PS 95.45, and TPS 95.45. These specimens were analyzed to determine the impact of tool parameters on the flow of material in the weld. Table 2 demonstrates that both threads and scrolls have an impact on increasing flow band width, though threads have a much larger impact.

Table 2 - Flow Band Width by Tool Feature

Name	Rotation Rate (RPM)	Transverse Rate (mm/min)	Measured Flow Band Width (mm)	Predicted Flow Band Width (mm)	Error
PS Sample	1400	152.4	3.81	4.99	30.89%
TP Sample	1400	152.4	4.44	4.99	12.36%
TPS Sample	1400	152.4	4.49	4.99	11.06%

9.2 Axial Force

Several trends or observations that span entire welds will be made here, but this data will later be localized to the area where each specimen was taken to find the mechanical conditions that contributed to the specimen’s strength. Three key observations can be made about the axial force measurements. The first is the rank of the magnitude of the axial forces between the tools. The TPS-t tool has axial force results on the order of half of the values for other tools, ranging from as low as 4000 N to 12,000 N. The TPS-t tool also sees the largest increase in axial force between individual welds. The PS tool ranges from 6000 to 14,000 N with weld three differing greatly from the first two. The TP tool ranged from 8000 to 12,000 N. Finally, the TPS tool had the largest axial forces, ranging from 10,000 N to 17,000 N.

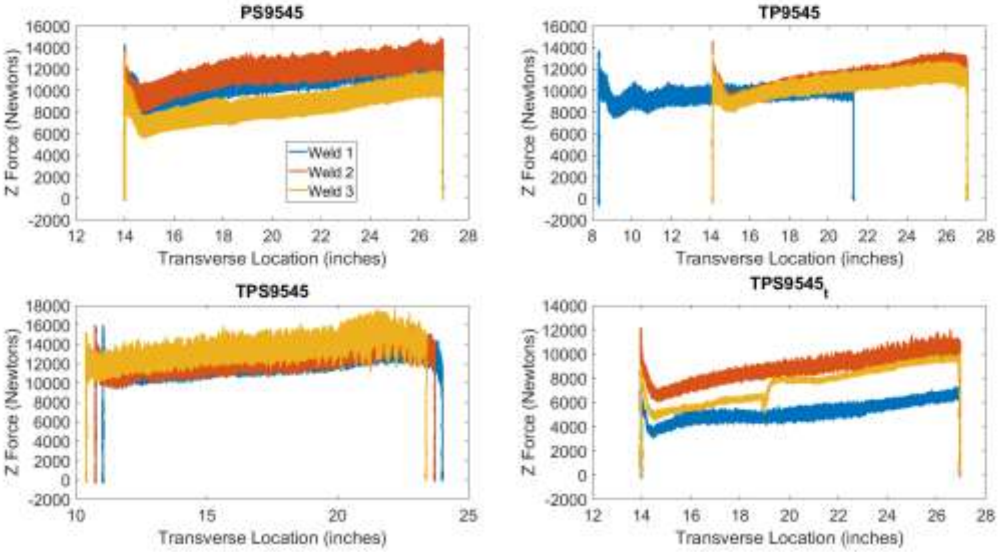

Figure 22 - Raw Axial Force Weld Data

Most welds exhibit an increase in axial force over the course of the weld. This has been attributed to thermal expansion of the material earlier in this thesis. Weld 1 using the TP tool was purposely welded at a location that utilized the low point of the anvil’s topography to examine the effect this may have on weld quality. The dip in the anvil topography occurs at about 10 inches for reference in Figure 22. The increase in axial force across most individual welds is approximately 2000 N, but some of this can also be attributed to rising anvil topography.

It is obvious from the force data that the pin broke off around a transverse location of 19 inches on the third weld for TPS 9545_t. The axial forces during the second weld were nearly double the first weld which may have contributed to the pin breaking. The force data for the third weld has a discontinuity increase from about 6000 N to 8000 N, but otherwise seems unaffected by the event. The process seems to attempt to self-regulate with the new circumstances of the weld. It is unknown but interesting why an absence of a pin would increase the axial force.

The final observation concerns the magnitude of periodic axial force oscillations between the tools. Again, the TPS-t tool exhibited behavior drastically less than the other tools, at no more than 1000 N oscillations. The TP tool exhibited oscillations roughly 2000 N in magnitude. The PS and TPS tools both exhibited oscillations roughly 4000 N in magnitude.

Interestingly, when the axial force at the specimen locations is compared with the specimen yield strength, there are clear areas that each tool exists in that become even clearer in measurements below. The TP 9545 tool generally experiences more axial force at about 12,000 N, the TPS tool experiences about 10,000 N, and the TPS9545_t tool experiences the least at a range from 5000-9000 N. The PS 9545 tool is very nonuniform with axial forces ranging from 7000-12,000 N. There does not appear to be an optimal value for axial force concerning resulting yield strength.

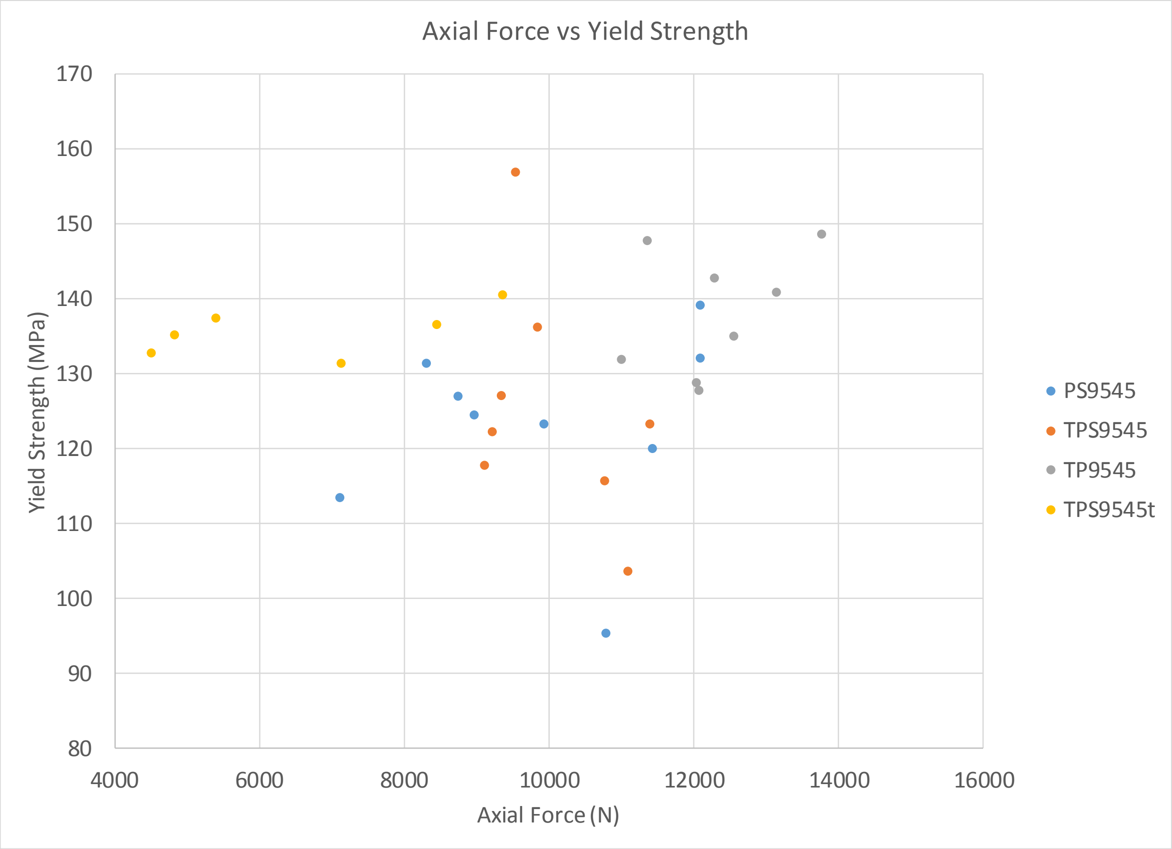

Figure 23 - Axial Force at Specimen Locations

9.3 Transverse Force

Forces are measured with an axis rotating with the tool. The transverse force can be calculated using both the rotating x and y force measurements, but oscillations at various frequencies make the results questionable. The measured magnitude should be at a maximum value when the measured force in the x direction lines up with the stationary axis of the moving table and at an equally negative value when the axis is 180 degrees out of phase. The maximum and minimum values averaged over every 100 data points is shown in Figure 24. The maximum magnitudes were used for transverse forces exhibited at the specimen locations. The magnitudes of the maximum and minimum values are not equal, and the magnitude of the minimum value is usually greater. This could be caused by a slight misalignment of the tool in relation to the anvil or descriptive of the material sticking to the tool for part of the rotation.

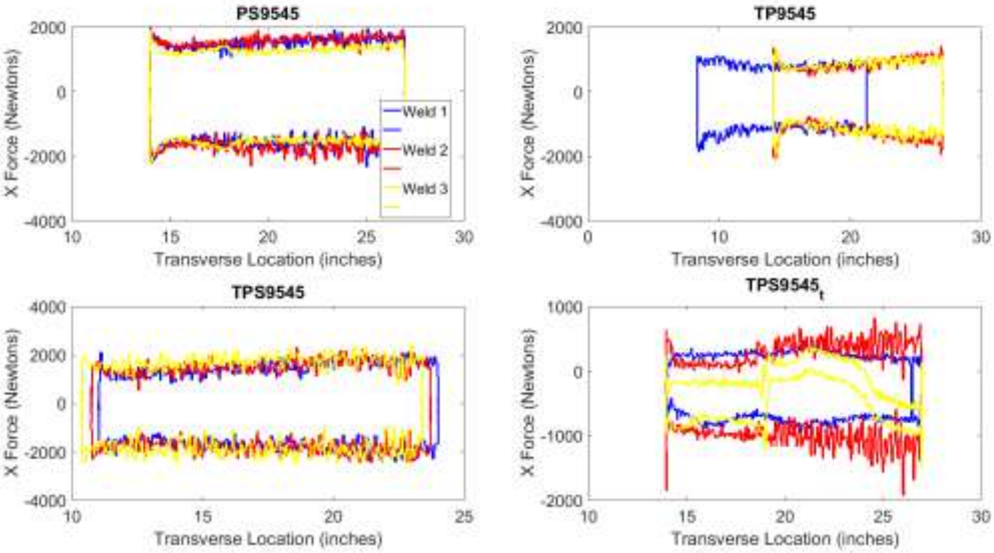

Figure 24 - Transverse Force Minima and Maxima

Transverse forces are much more constant across the length of a weld, from one weld to another, and across different tools. Both TPS 9545 and PS9545 exhibit transverse forces around 1500 N, while TP 9545 only exhibits transverse forces around 1000 N. Scrolls appear to increase the required transverse force by 500 N. The triangular pin tool exhibits much lower forces than the circular tools. The first two welds oscillated between about 250 N to -600 N, displaying a much more pronounced asymmetry than the other tools as well. The pin breaking is very evident in the third weld, and an unexpected transient behavior is displayed after this event. During the second weld, at about the 18 inch location the transverse force data becomes more erratic signaling the initial weakening of the joint between the pin and the shoulder. It appears an internal fracture occurred in the pin during the second weld, but the pin did not actually break off until the third weld.

When the transverse forces at the specimen locations are examined there is a similar grouping of tool values found as was noticed in axial forces at specimen locations. The PS 9545 and TPS 9545 tools demonstrate the largest magnitude of transverse forces ranging from 1100 to

1600 N and 1500 to 2000 N respectively. The TP 9545 and TPS 9545_t transverse forces demonstrate much lower magnitudes at 700 to 1100 N and 150 to 350 N respectively.

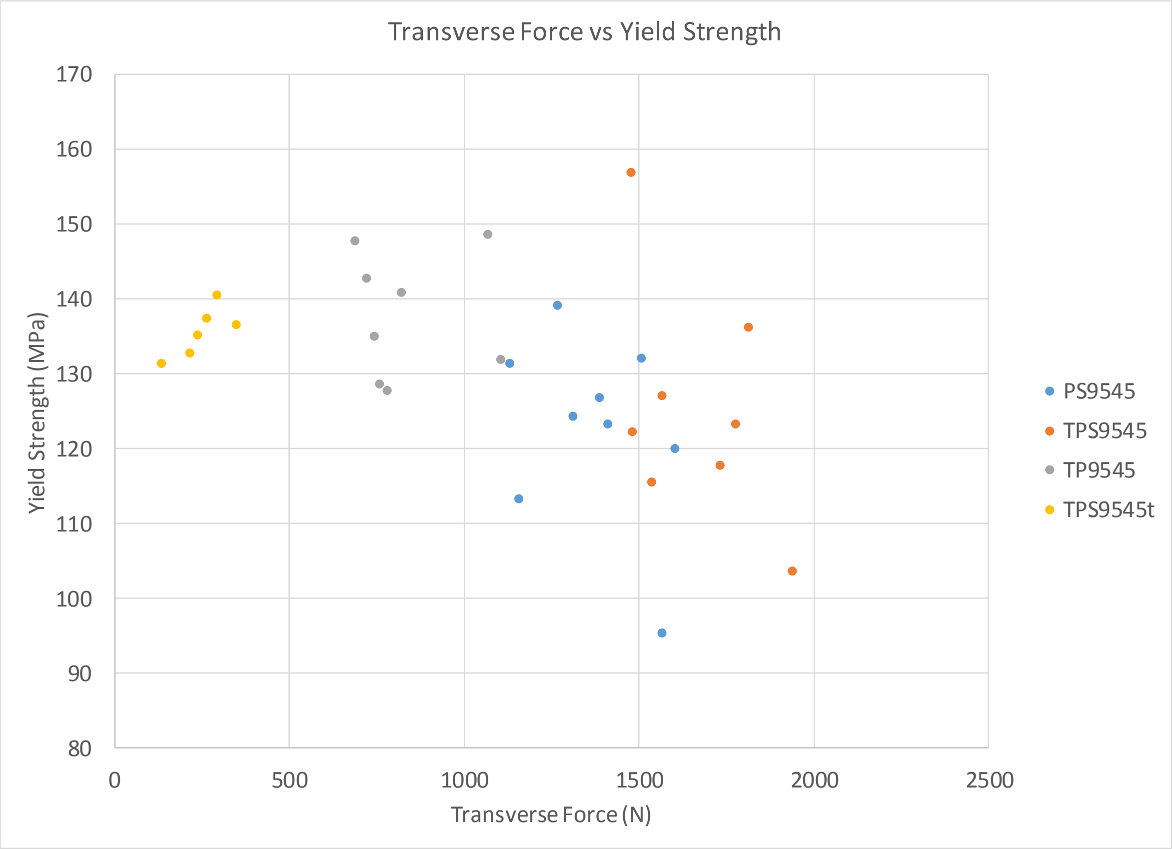

Figure 25 - Transverse Force at Specimen Locations

9.4 Torque

Torque across an entire weld varied slightly between circular pins and drastically for the triangular pin. The TP 9545 tool exhibited the least maximum torque at 20 N-m, followed by PS 9545 at 30 N-m, and finally TPS 9545 at 35 to 40 N-m. The triangular pin exhibited much lower maximum torques at around 11.5 N-m, with the effects of the pin breaking off very apparent.

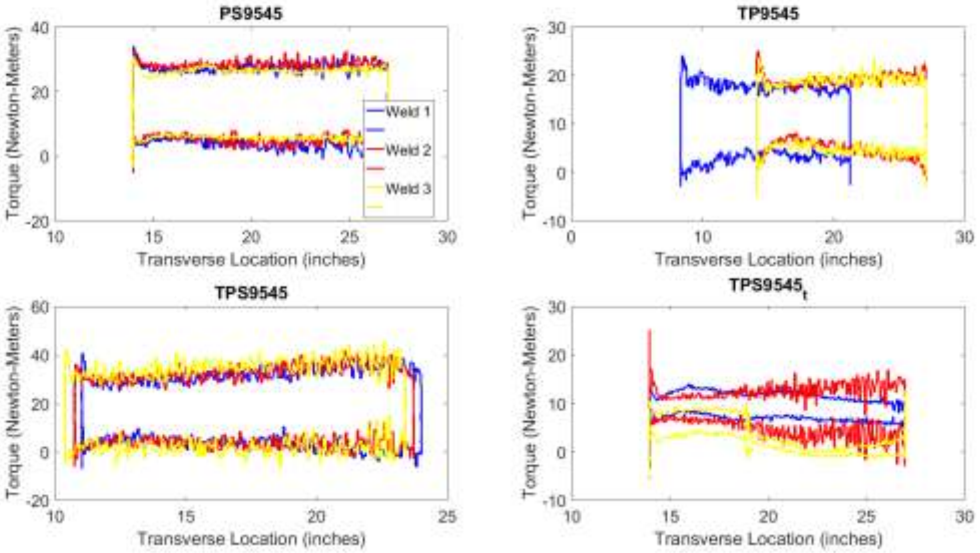

Figure 26 - Torque Minima and Maxima

The torque oscillates between two torque values, and the maximum torque value is potentially the more interesting value. The tool applies torque until the material yields while the material is sticking to the tool. The tool then either slips or the viscosity of the material decreases until it is plastic enough to flow. The maximum torque would be the torque applied to achieve the flow stress of the material. The torque for PS 9545 is 25 to 32 N-m, TP 9545 is around 16 to 22 N-m, TPS 9545 is erratic varying from 28 to 41 N-m. The first weld for the triangular tool has a uniform maximum torque around 11.5 N-m, the lowest of all the tools, and the lowest difference between maximum and minimum torque values. The second weld displays similar behavior to the first weld until about the 18 inch mark and then shows increasing magnitudes of oscillation. The third weld demonstrates torque values similar to the first weld until about the 19 inch mark when the pin obviously breaks and the torque magnitude of oscillation and maximum torque values greatly reduce to negligible values.

The strongest relationship between in-process measurements and resulting yield strength occurs for torque. There is an inversely proportional relationship between torque and yield strength. As torque increases, yield strength decreases. The values in Figure 27 are the maximum torque values where the specimen was taken. The tools exhibit distinct, vertical bands of torque values. The triangular tool exhibits the widest range of torque values from 0 to 12 N-m, but only because of the pin breaking. If the third weld's values are discounted, the triangular tool has the most uniform values at 11.5 with a standard deviation of only 0.27 N-m. The TPS tool from 31 to 36 N-m, the PS tool from 26 to 29 N-m, and the TP tool from 16 to 20 N-m.

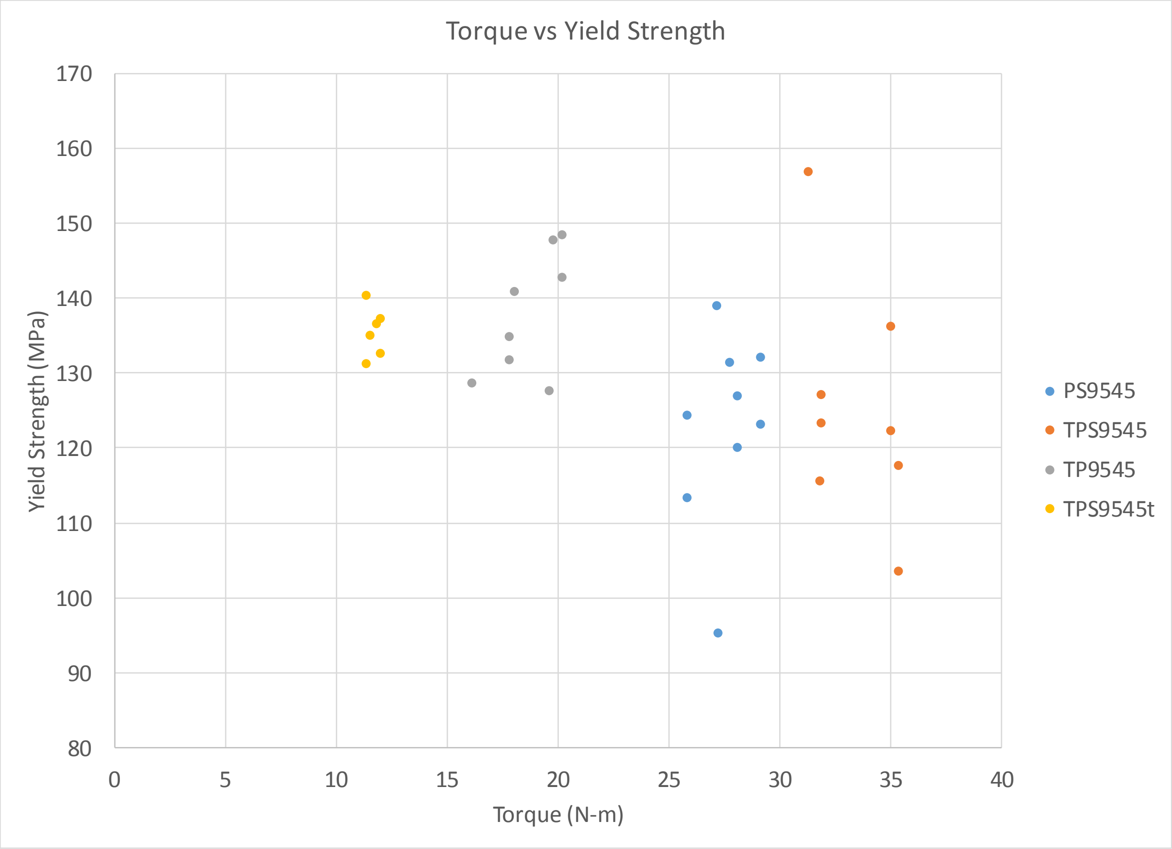

Figure 27 - Torque at Specimen Locations

9.5 Yield Strength

Yield strengths were calculated using the 0.2% offset method and the following figures show each weld's stress-strain curve and associated offset intersect line. The moduli are generally similar among the same welds and across different welds with the same tool. This demonstrates that the data is acceptable overall and is a factor for excluding outliers when this is not true. For example, in weld 2 of Figure 29 the center specimen (TP 9545_2VC) is much greater than the strengths of all other specimen for the same tool. This data was excluded as an outlier for many reasons including the large difference in this specimen's modulus. The left specimen in Figure 30 (TPS 9545_5VL) was also excluded as a low outlier for the same reasons. The final weld for the triangular tool (TPS 9545_t_3VC, TPS 9545_t_3VL, TPS 9545_t_3VR) was also excluded because a successful weld was not achieved after the pin broke.

It is likely that the erroneous data occurred during tensile testing. Our samples were three inches in width, and the extensometer used was a little over one inch wide. This did not leave much material for the grips to affix to. This lead to some specimens failing at the grip interfaces instead of in the material. Future specimens should be wider to avoid this issue.

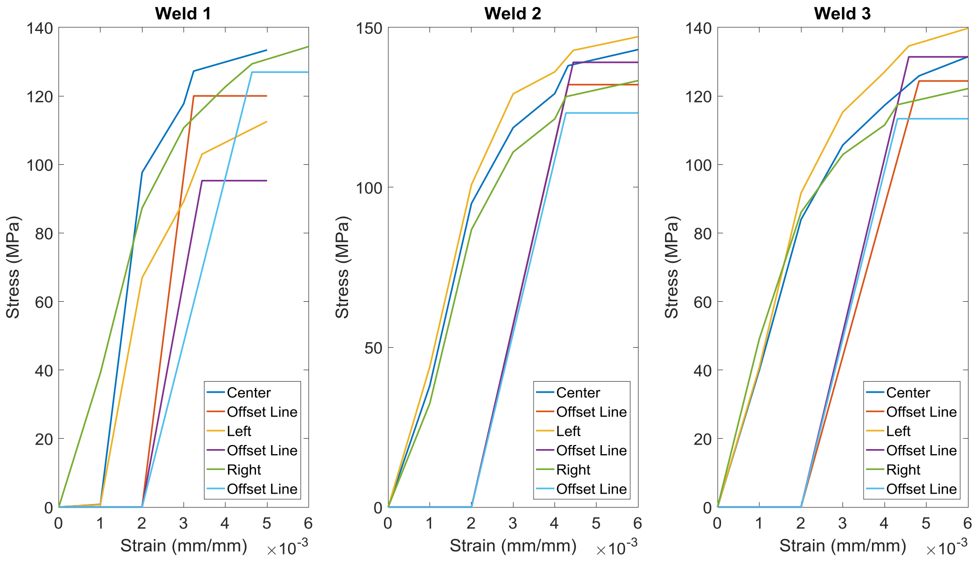

Figure 28 - PS 9545 Tensile Test Results

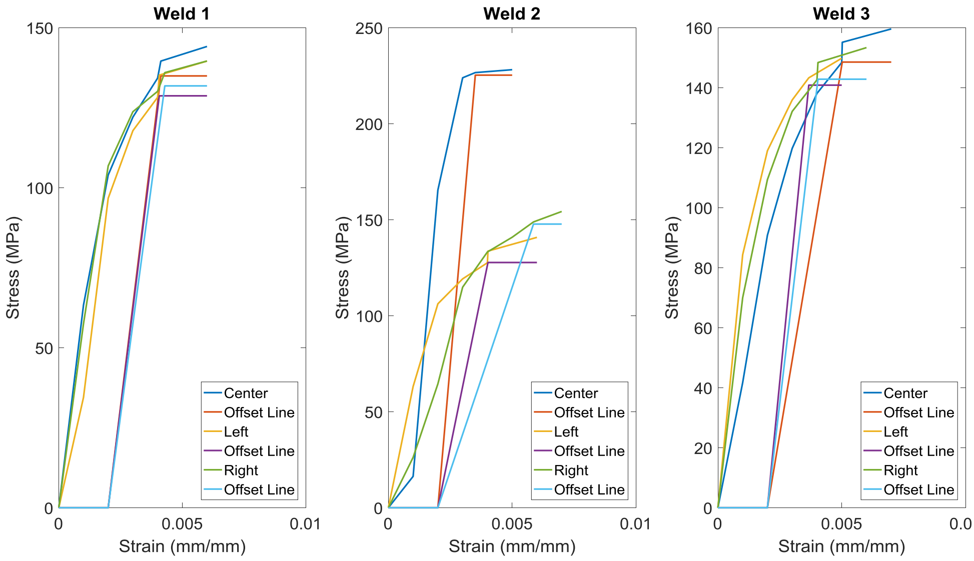

Figure 29 - TP 9545 Tensile Test Results

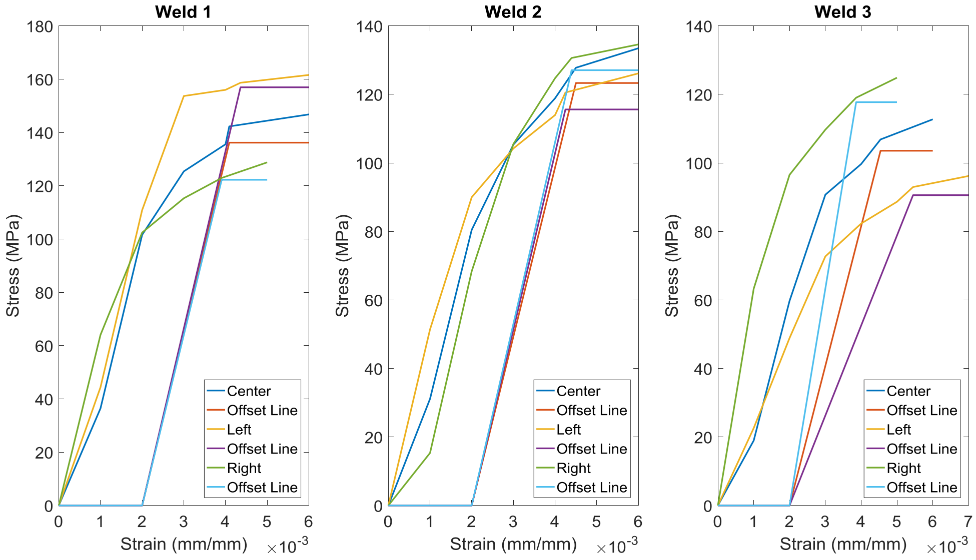

Figure 30 - TPS 9545 Tensile Test Results

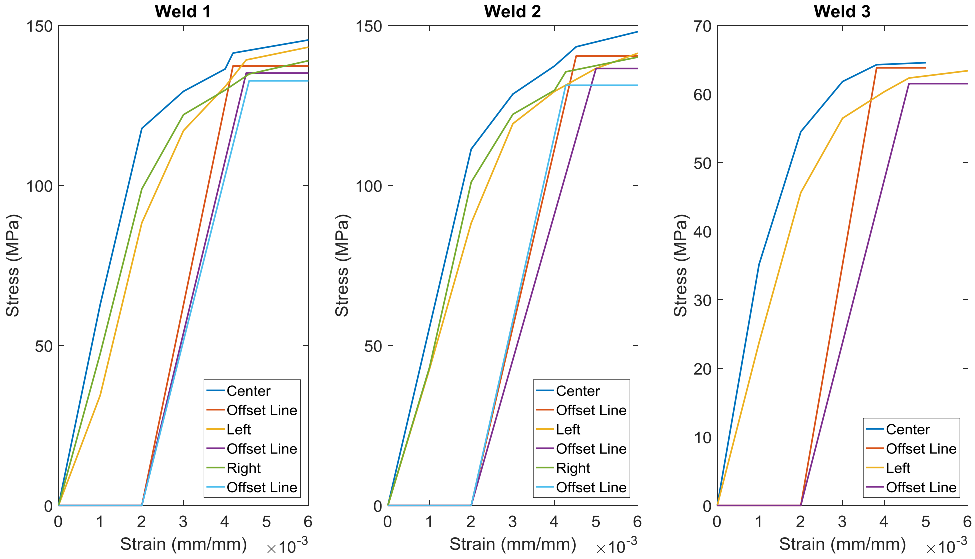

Figure 31 - TPS 9545-t Tensile Test Results

A summary of moduli, strengths, and mechanical conditions for all specimens is shown in Table 3. The welds are color coded according to the number weld they were in a session of welding to account for thermal affects that might occur if the tool and anvil had not returned to room temperature. For example, all the TPS 9545 welds were conducted in one day during a single session but required two test welds were performed to test weld parameters. The two test welds were weld numbers one and two of the session, and the first official weld was the third weld of the session. No significant trends could be identified with the small amount of data associated with weld number.

Table 3 - Raw Specimen Test Data

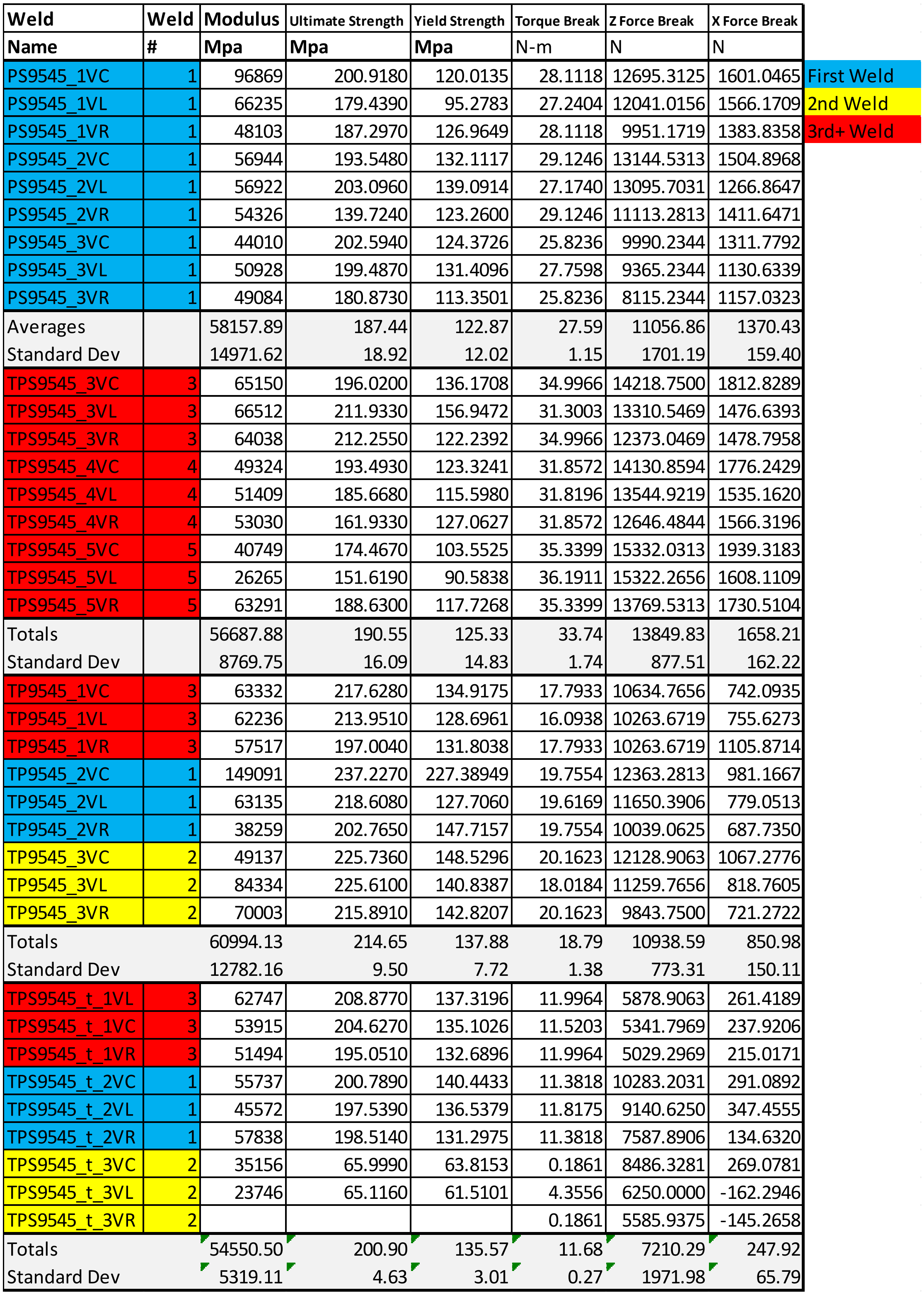

Weld	Weld	Modulus	Ultimate Strength	Yield Strength	Torque Break	Z Force Break	X Force Break
Name	#	Mpa	Mpa	Mpa	N-m	N	N
PS9545_1VC	1	96869	200.9180	120.0135	28.1118	12695.3125	1601.0465
PS9545_1VL	1	66235	179.4390	95.2783	27.2404	12041.0156	1566.1709
PS9545_1VR	1	48103	187.2970	126.9649	28.1118	9951.1719	1383.8358
PS9545_2VC	1	56944	193.5480	132.1117	29.1246	13144.5313	1504.8968
PS9545_2VL	1	56922	203.0960	139.0914	27.1740	13095.7031	1266.8647
PS9545_2VR	1	54326	139.7240	123.2600	29.1246	11113.2813	1411.6471
PS9545_3VC	1	44010	202.5940	124.3726	25.8236	9990.2344	1311.7792
PS9545_3VL	1	50928	199.4870	131.4096	27.7598	9365.2344	1130.6339
PS9545_3VR	1	49084	180.8730	113.3501	25.8236	8115.2344	1157.0323
Averages		58157.89	187.44	122.87	27.59	11056.86	1370.43
Standard Dev		14971.62	18.92	12.02	1.15	1701.19	159.40
TPS9545_3VC	3	65150	196.0200	136.1708	34.9966	14218.7500	1812.8289
TPS9545_3VL	3	66512	211.9330	156.9472	31.3003	13310.5469	1476.6393
TPS9545_3VR	3	64038	212.2550	122.2392	34.9966	12373.0469	1478.7958
TPS9545_4VC	4	49324	193.4930	123.3241	31.8572	14130.8594	1776.2429
TPS9545_4VL	4	51409	185.6680	115.5980	31.8196	13544.9219	1535.1620
TPS9545_4VR	4	53030	161.9330	127.0627	31.8572	12646.4844	1566.3196
TPS9545_5VC	5	40749	174.4670	103.5525	35.3399	15332.0313	1939.3183
TPS9545_5VL	5	26265	151.6190	90.5838	36.1911	15322.2656	1608.1109
TPS9545_5VR	5	63291	188.6300	117.7268	35.3399	13769.5313	1730.5104
Totals		56687.88	190.55	125.33	33.74	13849.83	1658.21
Standard Dev		8769.75	16.09	14.83	1.74	877.51	162.22
TP9545_1VC	3	63332	217.6280	134.9175	17.7933	10634.7656	742.0935
TP9545_1VL	3	62236	213.9510	128.6961	16.0938	10263.6719	755.6273
TP9545_1VR	3	57517	197.0040	131.8038	17.7933	10263.6719	1105.8714
TP9545_2VC	1	149091	237.2270	227.38949	19.7554	12363.2813	981.1667
TP9545_2VL	1	63135	218.6080	127.7060	19.6169	11650.3906	779.0513
TP9545_2VR	1	38259	202.7650	147.7157	19.7554	10039.0625	687.7350
TP9545_3VC	2	49137	225.7360	148.5296	20.1623	12128.9063	1067.2776
TP9545_3VL	2	84334	225.6100	140.8387	18.0184	11259.7656	818.7605
TP9545_3VR	2	70003	215.8910	142.8207	20.1623	9843.7500	721.2722
Totals		60994.13	214.65	137.88	18.79	10938.59	850.98
Standard Dev		12782.16	9.50	7.72	1.38	773.31	150.11
TPS9545_t_1VL	3	62747	208.8770	137.3196	11.9964	5878.9063	261.4189
TPS9545_t_1VC	3	53915	204.6270	135.1026	11.5203	5341.7969	237.9206
TPS9545_t_1VR	3	51494	195.0510	132.6896	11.9964	5029.2969	215.0171
TPS9545_t_2VC	1	55737	200.7890	140.4433	11.3818	10283.2031	291.0892
TPS9545_t_2VL	1	45572	197.5390	136.5379	11.8175	9140.6250	347.4555
TPS9545_t_2VR	1	57838	198.5140	131.2975	11.3818	7587.8906	134.6320
TPS9545_t_3VC	2	35156	65.9990	63.8153	0.1861	8486.3281	269.0781
TPS9545_t_3VL	2	23746	65.1160	61.5101	4.3556	6250.0000	-162.2946
TPS9545_t_3VR	2				0.1861	5585.9375	-145.2658
Totals		54550.50	200.90	135.57	11.68	7210.29	247.92
Standard Dev		5319.11	4.63	3.01	0.27	1971.98	65.79

First Weld
2nd Weld
3rd+ Weld

Table 4 shows a simple analysis of the average yield strength, standard deviation, and coefficient of variance across all tools. The TP 9545 tool resulted in the highest average strength, the TPS 9545 tool exhibited the largest standard deviation, and the TPS 9545_t tool exhibited the lowest standard deviation. Coefficients of variance ranged from just over 2% for the TPS_9545_t tool to almost 12% for the TPS 9545 tool.

Table 4 - Tool Result Analysis

AVG PS	St Dev	Coef of Var	AVG TPS	St Dev	Coef of Var	AVG TP	St Dev	Coef of Var	AVG TPS_t	St Dev	Coef of Var
122.87	12.02	9.78%	125.33	14.83	11.84%	137.88	7.72	5.60%	135.57	3.01	2.22%

Finally, Table 5 attempts to describe any effect of anvil topography on the strength of welds across all tools. Overall, specimens taken from the right side (near the beginning) of the weld were weaker by 1-2 MPa. This trend was stronger for the TPS 9545 and TPS 9545_t tools, while the TP 9545 demonstrated stronger than average strengths on the right. The strongest location for all tools but TPS 9545 was in the center, but the strongest location across all tools was the left side.

Table 5 - Specimen Location Result Analysis

Mean Left	St Dev	Coef of Var	Mean Center	St Dev	Coef of Var	Mean Right	St Dev	Coef of Var
Overall								
130.72	15.53	11.88%	130.08	12.03	9.25%	128.81	10.10	7.84%
PS 9545								
121.93	19.10	15.67%	125.50	5.00	3.99%	121.19	5.75	4.74%
TPS 9545								
136.27	20.67	15.17%	121.02	13.42	11.09%	122.34	3.81	3.12%
TP 9545								
132.41	5.97	4.51%	141.72	6.81	4.80%	140.78	6.65	4.73%
TPS 9545_t								
135.82	0.72	0.53%	138.88	1.56	1.12%	131.99	0.70	0.53%

The relationship between location of specimen and strength may be better characterized by Table 6. The mean strengths at each location were divided by the overall mean strength for each tool. This allows better comparisons between different tools. This table makes it apparent that the TP 9545 exhibits a unique trend from all other tools.

Table 6 - Percentage of Mean Strength by Specimen Location

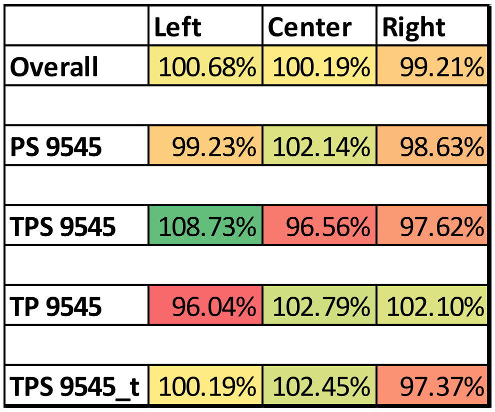

	Left	Center	Right
Overall	100.68%	100.19%	99.21%
PS 9545	99.23%	102.14%	98.63%
TPS 9545	108.73%	96.56%	97.62%
TP 9545	96.04%	102.79%	102.10%
TPS 9545_t	100.19%	102.45%	97.37%

10. Discussion

10.1 Tool Features Effect on Transverse Force

The standard tool for comparisons will be the TPS 9545. The threadless PS 9545 tool exhibited transverse forces almost 300 N less than the standard tool with a standard deviation almost identical to the standard tool. The threads increase strain rate by creating vertical flow. This could decrease viscosity of the material slightly and consequently decrease transverse forces. This vertical flow is eventually impeded by the anvil and forced horizontally. This horizontal flow seems to dominate the decrease in viscosity created and result in an increase in transverse forces when using threads. The almost identical standard deviation to the standard tool signals that threads do not contribute to orderly flow in the plasticized region.

The TP 9545 tool without scrolls exhibited transverse forces more than 800 N less than the standard tool with a standard deviation less than the standard tool. This demonstrates that scrolls play a large part in increased transverse forces. The scrolls direct colder material at the outside of the weld zone towards the pin to be strained and warmed to lower viscosity. This increases the flow band zone and affects the dynamic recrystallized zone shape which will be further discussed in a later section. The cost of driving this colder material towards the pin is increased transverse forces, which is demonstrated by these results.

The triangular pin tool exhibited transverse forces over 1500 N less than the standard tool with a standard deviation much less than the standard tool. Flow past a confined rotating circular cylinder is prone to vortex shedding which creates fluctuating pressures in the cylinder's wake. [39] The high rotation rate and low Reynolds number tend to reduce vortex shedding and increase Magnus effect forces which also affects flow behind the pin. Though vortex shedding may not occur under FSW conditions, the inhibition of boundary layer separation has been shown. [40] This explains the recirculation of material around the pin. Turbulence could result from vortex shedding or the outer layer of recirculated material interacting with stationary parent material. This turbulence combined with oscillations between sticking and slipping could contribute to turbulent mechanical conditions behind the pin and high standard deviations resulting in strength. In contrast, a triangular pin separates plasticized material into orderly packets with smaller vortices and smaller pressure fluctuations in its wake. This lack of turbulence could translate to lower standard deviation in transverse forces for triangular pin tools.

10.2 Tool Features Effect on Axial Force

The threadless PS 9545 tool exhibits axial forces almost 3000 N less than the standard tool at a standard deviation almost twice that of the standard tool. The decrease in axial forces is expected since threads drive material downward and increase axial forces. The threads also create more predictable vertical flow, causing less variance in axial force.

The unscrolled TP 9545 tool exhibits axial forces almost 300 N less than the standard tool at a standard deviation more than 100 N less than the standard tool. The scrolls direct material back towards the pin which results in increased axial forces, but the results show that this effect is not anywhere near the effect that pins have on axial force. The unscrolled tool allows material to escape the shoulder which slightly reduces axial forces.

The triangular pin TPS 9545_t tool exhibits axial forces more than 6500 N less than the standard tool at a standard deviation over 1000 N more than the standard tool. The values for the first weld alone, discounting the second weld that had a weakening pin, displays axial forces more than 8000 N less than the standard tool and a standard deviation more than 500 N less than the standard tool. The weakening pin obviously contributed to fluctuating axial forces, but if the data from the first weld alone is used the TPS 9545_t tool has drastic reductions in magnitude and oscillations of axial forces. Like with the transverse forces, this may be a result of laminar flow because vortexes are not formed as with the circular pin. This explains why both the magnitude and the standard deviation of axial forces is much lower.

10.3 Tool Features Effect on Torque

The threadless PS 9545 tool exhibited torques more than 6 N-m less than the standard tool and a standard deviation more than 0.5 N-m less than the standard tool. The torque is likely heavily influenced by the axial force, but this does not entirely account for torque values. The PS 9545 and TP 9545 tools had similar axial force values but differ greatly in torque values. While the PS 9545 tool had the greatest standard deviation for axial force, only the triangular tool has a smaller standard deviation for torque. The threads induce vertical flow and vertical strain which can reduce viscosity. The reduced viscosity means more material is plasticized and rotated with the tool. This increased material requires more torque for the tool to rotate. Since there is less plasticized material without a threaded tool, the amount of plasticized material varies less and results in a smaller standard deviation for torque.

The unscrolled TP 9545 tool exhibited torques almost 15 N-m less than the standard tool and a standard deviation almost 0.5 N-m less than the standard tool. Scrolls direct denser material back toward the pin requiring torque to rotate it. Without the scrolls, material is allowed to escape which greatly reduces torque required by the machine. The parameters used in this experiment likely produce too much plasticized material, so allowing material to escape is beneficial at these conditions. If the heat input is reduced, an unscrolled tool may allow too much material to escape and fail to be consolidated behind the pin.

The triangular TPS 9545_t tool exhibited torques more than 22 N-m less than the standard tool and a standard deviation about 15% of the standard tool. This is likely a compounding effect of both lower axial and transverse forces achieved through more laminar flow when compared to circular pins.

10.4 Tool Features Effect on Yield Strength

The threadless PS 9545 tool had the lowest yield strength of all the tools. This demonstrates the importance of threads to effective material flow. Without threads to drive the material downward, excess material accumulates at the top of the weld and is expelled as flash. [38] This tool also had higher standard deviations for in process forces and yield strength suggesting a correlation between turbulent flow and resulting weld strength. Interestingly, it had a low standard deviation for torque. Torque magnitude may be a slight indication of weld strength, though oscillations in weld magnitude do not seem to affect the process greatly.

The unscrolled TP 9545 tool demonstrated the highest yield strength of all the tools. This result may be an outlier due to the welding parameters used for this experiment. In comparison with welding parameters of similar experiments, this experiment had higher rotation rates resulting in higher heat input. The TP 9545 tool does not direct excess material back towards the pin. This tool may not direct enough material back to the pin to be reconsolidated for lower heat input experiments. Excessive flash was observed with the PS 9545 tool suggesting that allowing some material to escape under these conditions is beneficial for flash reduction.

The triangular pin TPS 9545_t tool demonstrated strengths comparable to the TP 9545 tool at 135.57 MPa compared to 137.88 MPa respectively. The standard deviation of strengths for the triangular tool was also less than 40% of the TP 9545 tool results. This follows the trends from the earlier observations of in-process force oscillations causing more predictable, laminar flow.

The overall strengths of the welds are far below what a traditional welding parameter metric may predict. As was mentioned in section 5, the predicted weld strength using this experiment's parameters was about 140 MPa. Actual strengths range only from 122 to almost 138 MPa, and only 125 MPa for the standard tool. This was predicted by the proposed welding parameter metric in section 5. This lower strength may be a result of the material acting more like a liquid under such high heat input conditions. The temperature graph in Figure 17 also supports this idea. The temperature was held at the solidus temperature if the calculated temperature was greater than the solidus temperature. The graph demonstrates that the temperature is greater than the solidus temperature for a large portion of the flow band and may contribute to melting or phase changes in this region. Welding parameters should optimize the heat input to minimize this high temperature region of the weld zone. This explanation matches with previous conclusions by Crawford et al. and explains the observations of excess flash noticed using tool PS 9545. Tool TP 9545 may avoid excess flash by not drawing already heated material into the weld zone to be reheated to excess temperatures.

10.5 Tool Features Effect on Dynamic Recrystallized Zone Shape

Figure 32 shows the etches of the weld zone for all tools except TPS 9545_t. No etching was done for the TPS 9545_t tool because a suitable sample could not be made. This was an oversight and future work should cover the shape of the weld zone for a triangular pin. The heat affected zones, shown in dark gray, are similar for all welds. This is expected because this area is thought to be mainly influenced by the heat from the shoulder's rotation, and rotation rates for all specimen were the same. The right side of the dynamic recrystallized zone (DXZ), shown in the lighter gray inside the heat affected zone, all seem similar as well. The key differences between all samples is found in the shape of the left (retreating) side of the DXZ.

Sample PS

Sample TP

Sample TPS

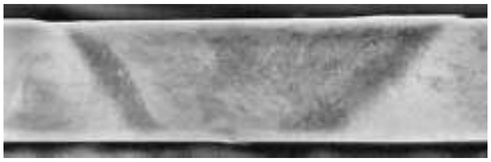

Figure 32 - Etches of Welds from Different Tools

The DXZ of the PS 9545 sample has an angle of about 45 degrees until halfway down to the root of the weld where a small vertical section is observed. This suggests that shoulder effects dominate the shape of the DXZ for this tool. This is expected since there are no threads to influence flow from the pin. The result is a much narrower DXZ. Since the DXZ is not the weakest part of the weld, a smaller cross-sectional area DXZ correlates to lower weld strength.

The DXZ of the TP 9545 sample is almost vertical and recedes near the top of the weld near the shoulder. There is no indication of any effect from the shoulder in the DXZ. This wider cross-sectional area of DXZ may correlate to the TP 9545 tool’s higher yield strengths, but it cannot be the sole reason because it was not the only tool with threads on the pin.

The DXZ for the standard TPS 9545 tool has a shape similar to the PS 9545 tool, but not as narrow. The angle changes to be more vertical in about the top quarter of the weld, resulting in more cross-sectional area for the DXZ. The cross section is similar to, if not greater than the cross-sectional area for the TP 9545 tool. It is hypothesized that the lack of scrolls actually benefitted the TP 9545 tool by not drawing in excess, overheated material to be consolidated into the weld or expelled as flash. The TPS 9545 tool may produce superior welds if the welding parameters lower heat input. Future work should be completed to confirm this hypothesis.

10.6 Tool Features Effect on Flow Band Width

Table 2 shows the comparison of the predicted flow band widths at the experimental welding parameters and the measured flow band widths for all tools except TPS 9545_t. These results confirm the observations made about the shape of the DXZ that the PS 9545 tool has the smallest flow band width, followed by TP 9545, and finally the TPS 9545.

The prediction of flow band widths using the model in this thesis is more accurate at higher energy depositions as shown in Figure 21. This may suggest that the viscosity model most accurately models that behave more like a fluid, similar to the Couette Flow model mentioned in section 3. This may also be caused by the assumption of a constant, temperature-compensated yield stress for calculating each weld’s heat generation as discussed earlier. A full model that can eliminate this assumption is needed to fully analyze this error trend. Future work should also focus on flow band volume instead of just width for more accurate results.

10.7 Mechanical Conditions and Weld Parameter Map

The figures using in-process forces from the approximate location in the weld where the specimen were taken is unique to the knowledge of the author. They provided more precise, granular knowledge of mechanical conditions at the locations where the weld was actually tested instead of vague forces averaged for the entire weld. This data gave insights that was not immediately apparent given then averaged forces data.

10.8 Thermal Expansion Controller

In an uncontrolled weld, as the topography of the material rises and falls, it causes the axial force to rise and fall proportionally. The axial force is responsible for heat generation from friction. The rise and fall will also change the amount that the shoulder of the tool is engaged in the material. If the topography of the weld is too high, excess heat and material engagement occurs. If the topography of the weld is too low, not enough friction is produced and the weld may not reach sufficient depth. From past experimental observations of our welding machine, the change in height of the material thought necessary to affect a weld is 0.005 inches. Traditional methods for controlling for this disturbance were to control the plunge depth motor to maintain a constant axial force.

Longhurst et al. [32] showed that plunge depth controllers struggle with axial force oscillations when the tool contacts the material, predicting penetration depth, and slow force calculations. A novel traverse speed controller was proposed that could vary traverse rate to control axial force and create uniform thermomechanical conditions along the entire weld. Axial force and traverse rate are inversely proportional, so as axial force began to increase, the controller decreased the traverse rate. This increased energy deposition, allowing the material to be heated, become less viscous, and flow at lower axial forces.

Longhurst attributed increasing axial force required to the tool moving into colder material [32], but this uses a micro observation to explain a macro trend. It is more likely that as the material heats up, it attempts to expand but is prevented in the axial direction partially by the clamping. This creates a positive force in the axial direction that the axial motor must counter. From Longhurst’s figure of a weld sample with no force control, the Z force rises from about 5900 N to 7200 N during the traverse section of the weld. He also notes that the thickness of the plate is 0.25 in and the tool increased 34 degrees Celsius in temperature over the weld. Using a rough 1D approximation of the thermal stress ($\sigma = E\alpha\Delta T$) the modulus of AL6061 is 68.9 GPa, the coefficient of thermal expansion is 24.3 x 10^{-6}. The resulting thermal stress is 56.9 MPa. The area of the 1 inch diameter tool perpendicular to the z axis is $5.067*10^{-4}$ meters squared. This means a distributed force due to thermal stress of about 28,000 N. These one-dimensional, linear approximations overshoot the actual value when it is considered that there is expansion in two other dimensions, the probability of maximum expansion is low, and that material is being deposited into a void behind the tool. These factors could plausibly explain the reduction in Z force by 95%. Stress caused by thermal expansion is a more plausible explanation of the 1300 N increase in Z force seen in his figure.

It was previously thought that heat from the weld was building up at the end of the material, and the temperature was causing too much material to be plasticized resulting in flash. The observation above may serve as a more accurate explanation for the increased flash. As the material expands in the axial direction, more axial force is being applied by the shoulder to counter the expansion which results in more friction and more temperature. Additionally, however, more material is being engaged by the tool as the material expands axially. The combination of too much energy deposited into the weld and more material than the weld parameters were designed for is likely the reason for the excess flash at the end of welds. A controller that maintained constant axial force by varying traverse rates should account for the thermal expansion and result in better quality welds. A more ambitious controller would vary rotational velocity to maintain a constant temperature, constant thermal expansion, and resulting constant axial force.

10.9 Database

One difficulty with analyzing and verifying new FSW models is a lack of available data. Welds must be done over a wide range of welding parameters and tools to verify a model. Since many models have been proposed over the last decade, these welds are redundant. The problem is that most data from verification welds of preceding models is not published with the model. The result is both an uncertainty about exact welding conditions for previous models and an inability to quickly verify new models without redoing welds.

Publishing large matrices of in-process forces and strength data with papers is not feasible. As part of this project, all welding data has been set up to automatically save to a Secure Shell (SSH) server. This is done by automatically capturing welding parameters and other key information about each weld conducted as metadata text files that are saved and linked to the welding data files as text files. They are then sent by SSH to a separate welding database computer. The files are then added to a Structured Query Language (SQL) database, so they are searchable from any computer with internet access and access to the server.

This database has been created to better preserve and organize internal Vanderbilt University Welding Automation Lab (VUWAL) data, but it is also open to any users who would like to contribute their data and share our data. The hope is to create an open source database of welding information that users can eventually use to simulate actual welds and accelerate the pace of discovery in FSW. Information about gaining access to this database can be obtained by contacting the author.

11. Conclusions

This thesis has performed an initial study of the critical viscosity model proposed by Nandan et al in relation to different tool features. Specifically, it has developed a simple model for predicting flow band width that agrees with experimental results. Along the way it has proposed a better metric for comparing welding parameters across different tool designs and materials and investigated the impact that tool features have on in-process forces.

Many improvements can be made on the assumptions made here. Instead of a moving line heat source assumption, a volumetric heat source like work presented by Eagar and Tsai [3] could be calculated at greater computational cost. The thickness of the plates to be butt welded could also be accounted for more accurately. In this work it was assumed that it was accounted for by the pin height to plate thickness ratio being adequate. This assumption can be better analyzed in further work, especially how it may change with different pin shapes and the effect of pin cone angles.

One conclusion from this study is that the ratio of shoulder diameter to pin diameter should be reduced. Larger pins will create higher strain rates at lower rotation rates at the cost of higher required torque. It is worth investigating how much distributed heat from the shoulder is needed, and what the minimum shoulder diameter required to consolidate plasticized material into the weld is.

It has been shown experimentally that the axial force increases over time. This is likely due to thermal expansion of the material over the course of the weld. This increase in axial force changes the thermomechanical conditions of the weld and can cause vast differences in microstructure and strength over the length of the same weld. A controller that accounts for this expansion is required to ensure that the same thermomechanical conditions exist across the entire weld.

I have avoided at any cost the slippery slope of creating a full model. The calculations in this thesis are the results of an oversimplified, steady-state, pseudo model. I would not consider this model sufficient for proving the efficacy of the Nandan Critical Viscosity model. A full model with more verification welds should completed as future work in this area. For example, an assumption that the solidus temperature is maintained at the interface between the pin and the material interface is made. Using a full thermal model, this assumption can be verified. A temperature-compensated yield stress is also assumed to calculate the heat generation from plastic dissipation, and the flow stress is later solved for based on a temperature calculated using the Rosenthal equation. The initial yield stress assumption could be calculated through iteration until it agrees with the final flow stress calculated using the temperature calculation. This iteration was neglected in this work for time and computational limitations. Further experimental work that can be done for the verification of the critical viscosity model is more verification welds over a wide range of welding parameters and verification welds using different materials with different critical viscosities.

This thesis has attempted to demonstrate the possible efficacy of Nandan’s critical viscosity model. This model has not been tested to the knowledge of the author. Models have historically been poor at describing FSW across the entire range of welding parameters. The questions essentially boils down to whether the material acts more like a solid or a liquid which determines the modeling fundamentals used. The issue with modeling may be that the material may be put under conditions on the verge of conversion of the material from a solid to a liquid, and that one model may not be capable of describing the behavior of material in both states. Data included in this thesis supports this conclusion. Couette flow is effective at describing high energy deposition welding parameters, but less accurately describes lower energy deposition welds. Couette flow may be more resistant to weld defects such as wormholes, but at the price of weld strength due to phase changes in the welded material. The resulting strength is still higher than traditional welding, so it produces an option for industry to choose higher reliability welds if the highest strength welds are not necessary

REFERENCES

[1] Thomas, W., Nicholas, E., Needham, J., Temple-Smith, P., Klaus We Kallee, S., & Dawes, C. (1991). *Great Britain Patent No. 2,306,366.*

[2] Crawford, R. (2005). *Parametric Quantification of Friction Stir Welding.* Nashville, TN: Vanderbilt University, Masters Thesis.

[3] Eagar, T. W., & Tsai, N.-S. (1983). Temperature Fields Produced by Traveling Heat Sources. *64th Annual AWS Convention* (pp. 346-355). Philadelphia, PA: Weld. Res. Suppl.

[4] Nandan, R., Roy, G., & Debroy, T. (2006). Numerical Simulation of Three-Dimensional Heat Transfer and Plastic Flow During Friction Stir Welding. *Metallurgical and Materials Transactions*, 1247-1259.

[5] Mendez, P. F., Tello, K. E., & Lienert, T. J. (2010). Scaling of coupled heat transfer and plastic deformation around the pin in friction stir welding. *Acta Materialia*, 6012-6026.

[6] Schmidt, H., Hattel, J., & and Wert, J. (2004). An analytical model for the heat generation in friction. *Modeling and Simulation in Material Science and Engineering*, 143-157.

[7] Schmidt, H., & Hattel, J. (2005). Modelling heat flow around tool probe in friction. *Science and Technology of Welding and Joining*, 176-186.

[8] Colegrove, P., Painter, M., Graham, D., & Miller, T. (2000). 3-dimensional flow and thermal modelling of the friction stir welding process. *2nd International Symposium on FSW.* Gothenburg, Sweden.

[9] Colligan, K. (1999). Material flow behavior during friction stir welding of aluminum. *The Welding Journal*, 229-237.

[10] Reynolds, A. (2000). Visualisation of material flow in an autogenous friction stir weld. *Science and Technology of Welding and Joining*, 120-124.

[11] Arbegast, W. J. (2008). A flow-partitioned deformation zone model for defect formation during friction stir welding. *Scripta Materialia*, 372-376.

[12] Ulysse, P. (2002). Three-dimensional modeling of the friction stir-welding process. *International Journal of Machine Tools & Manufacture*, 1549-1557.

[13] Sellars, C., & Tegart, W. (1972). Hot Workability. *International Metallurgical Reviews*, 1-24.

[14] Sheppard, T., & Wright, D. (1979). Determination of Flow Stress: Part 1 Constitutive Equation for Aluminum Alloys at Elevated Temperatures. *Metals Technology*, 215-223.

[15] Kuykendall, K. (2011). *An Evaluation of Constitutive Laws and their Ability to Predict Flow Stress over Large Variations in Temperature, Strain, and Strain Rate Characteristic of Friction Stir Welding.* Provo, UT: Brigham Young University, PhD Thesis.

[16] Nunes Jr., A., Bernstein, E., & McClure, J. (2000). A rotating plug model for friction stir welding. *81st AWS Annual Convention.* Chicago, IL: American Welding Society.

[17] Owolabi, G., Odeshi, A., Singh, M., & Bassim, M. (2007). Dynamic shear band formation in Aluminum 6061-T6 and Aluminumm 6061-T6/Al2O3 composites. *Materials Science and Engineering*, 114-119.

[18] Manes, A., Peroni, L., Scapin, M., & Giglio, M. (2011). Analysis of strain rate behavior of an Al 6061 T6 alloy. *Procedia Engineering*, 3477-3482.

[19] Pei, X. J., & Dong, P. S. (2014). Shear localisation modelling of friction stir weld formation process. *Science and Technology of Welding and Joining*, 416-426.

[20] Pei, X., & Dong, P. (2017). A selectively-coupled shear localization model for friction stir welding process window estimation. *International Journal of Machine Tools and Manufacture*, 89-104.

[21] Franke, D. J., Morrow, J. D., Zinn, M. R., Duffie, N. A., & Pfefferkorn, F. E. (2017). Experimental Determination of the Effective Viscosity of Plasticized Aluminum Alloy 6061-T6 during Friction Stir Welding. *Procedia Manufacturing*, 218-231.

[22] Barbot, S. (2017). On the relation between plasticity, friction, and geometry. Unpublished. 1-10.

[23] Remington, B., Allen, P., Bringa, E., Hawreliak, J., Ho, D., Lorenz, K., . . . Yaakobi, B. (2006). Material dynamics under extreme conditions of pressure and strain rate. *Material Science and Technology*, 474-488.

[24] Tongne, A., Jahazi, M., Feulvarch, E., & Desrayaud, C. (2015). Banded structures in friction stir welded Al alloys. *Journal of Materials Processing Technology*, 269-278.

[25] Guerra, M., Schmidt, C., McClure, J., Murr, L., & Nunes, A. (2003). Flow patterns during friction stir welding. *Materials Characterization*, 95-101.

[26] Tongne, A., Desrayaud, C., Jahazi, M., & Feulvarch, E. (2017). On material flow in Friction Stir Welded Al alloys. *Journal of Materials Processing Technology*, 284-296.

[27] Qian, J., Li, J., Xiong, J., Zhang, F., Li, W., & Lin, X. (2012). Periodic Variation of torque and its relation to interfacial sticking and slipping during friction stir welding. *Science of Technology of Welding and Joining*, 338-341.

[28] Lim, S., Kim, S., Lee, C.-G., & Kim, S. (2004). Tensile Behavior of Friction-Stir-Welded AL 6061-T651. *Metallurgical and Materials Transactions A*, 2829-2835.

[29] Liu, X., Sun, Y., Morisada, Y., & Fujii, H. (2018). Dynamics of rotational flow in friction stir welding of aluminium alloys. *Journal of Materials Processing Tech.*, 643-651.

[30] Trueba Jr., L., Heredia, G., Rybicki, D., & Johannes, L. B. (2015). Effect of tool shoulder features on defects and tensile properties of friction stir welded aluminum 6061-T6. *Journal of Materials Processing Technology*, 271-277.

[31] Arbegast, W. J. (2003). Friction Stir Joining: Characteristic Defects. *Advanced Materials Processing Center*.

[32] Longhurst, W. R., Strauss, A. M., & Cook, G. E. (2010). Enabling Automation of Friction Stir Welding: The Modulation of Weld Seam Input Energy by Traverse Speed Force Control. *Journal of Dynamic Systems, Measurement, and Control*, 041002(11).

[33] Fuller, C. B. (2007). Friction Stir Tooling: Tool Materials and Designs. In R. S. Mishra, & M. W. Mahoney, *Friction Stir Welding and Processing* (pp. 7-35). Materials Park, OH: ASM International.

[34] Colegrove, P., & Shercliff, H. (2004). Development of Trivex friction stir welding tool: Part 1 - two-dimensional flow modelling and experimental validation. *Science and Technology of Welding and Joining*, 345-351.

[35] Colegrove, P., & Shercliff, H. (2004). Development of Trivex friction stir welding tool: Part 2 - three-dimensional flow modelling. *Science and Technology of Welding and Joining*, 352-361.

[36] Venkatesh, Arivarsu, Manikandan, & Arivazhagan. (2018) Review on friction stir welding of steels. *Materials Today*, 13227-13235.

[37] Jacquin, D., de Meester, B., Simar, A., Deloison, D., Montheillet, F., & Desrayaud, C. (2011). A Simple Eulerian thermomechanical modeling of friction stir welding. *Journal of Materials Processing Technology*, 57-65.

[38] Chen, G., Li, H., Wang, G., Guo, Z., Zhang, S., Dai, Q., . . . Shi, Q. (2018). Effects of pin thread on the in-process material flow behavior during friction stir welding: A computational fluid dynamics study. *International Journal of Machine Tools and Manufacture*, 12-21.

[39] Champmartin, S., Ambari, A., & Roussel, N. (2007). Flow around a confined rotating cylinder at small Reynolds number. *Physics of Fluids*, 103101.1-9.

[40] Kang, S., Choi, H., & Lee, S. (1999). Laminar flow past a rotating circular cylinder. *Physics of Fluids*, 3312-3321.